Reliability of inelastic wind excited structures by dynamic shakedown and adaptive fast nonlinear analysis (AFNA)

Bowei Li^a, Wei-Chu Chuang^b, Seymour M.J. Spence^{a,1,*}

^aDepartment of Civil and Environmental Engineering, University of Michigan, Ann Arbor, MI 48109, USA

^bMagnusson Klemencic Associates, 1301 Fifth Avenue, Suite 3200, Seattle, WA 98101, USA

Abstract

The ever-growing interest in performance-based wind engineering has created a need for assessment frameworks that can efficiently deal with inelasticity. The computationally efficient strain-driven dynamic shakedown approach has provided a solution that is not only capable of identifying failure mechanisms that are potentially critical during extreme winds, e.g., low cycle fatigue and ratcheting, but also allows direct estimation of inelastic deformations. This approach, however, can only solve problems at dynamic shakedown, i.e., with limited nonlinearity, and is not capable of providing response time histories. To address these limitations, this paper presents an efficient framework for reliability assessment of inelastic structures at dynamic shakedown and beyond. To this end, a novel step-by-step integration algorithm is developed for rapid response time history analysis within the setting of dynamic shakedown. The method is based on advancing fast nonlinear analysis through introducing schemes for enabling at each time step the adaptive selection of the step size, number of modes to be included, and number of potentially nonlinear elements. Inelasticity is modeled as distributed at the level of the stress resultants through a return mapping scheme based on the Haar-Karman principle, therefore enabling the integrated estimation of the state of dynamic shakedown. The scheme is seen to preserve the efficiency of recently developed strain-driven dynamic shakedown algorithms while providing a full range of response time histories at and beyond the state of dynamic shakedown. To enable reliability analysis, the scheme is embedded in a general uncertainty propagation framework.

^{*}Corresponding author

Email addresses: jacklbw@umich.edu (Bowei Li), WChuang@mka.com (Wei-Chu Chuang), smjs@umich.edu (Seymour M.J. Spence)

¹Tel. +1-734-764-8419, Fax +1-734-764-4292

Keywords: Wind reliability analysis, Inelastic wind analysis, Dynamic integration schemes, Distributed plasticity, Uncertainty propagation, Performance-based wind engineering

1. Introduction

With the recent introduction of performance-based wind engineering, the potential of designing wind-excited buildings with controlled inelasticity at ultimate load levels has attracted strong interest among practicing engineers [1]. Since the majority of current performance assessment procedures for wind excited structures are based on linear elastic analysis, the reliability of wind excited systems experiencing inelasticity must be carefully investigated to ensure safety against any undesirable failure scenarios. To estimate the reliability of such systems while treating general high-dimensional uncertainty, e.g., the stochasticity associated with the record-to-record variability in the external dynamic wind loads as well as the randomness in the model parameters, schemes based on stochastic simulation are generally required [e.g. 2, 3, 4, 5, 6, 7, 8, 9, 10, 11, 12], with the exception of the approach recently proposed in [13]. Notwithstanding the use of variance reduction methods for estimation of failure associated with rare events, e.g., stratified sampling [14], the computational feasibility of schemes based on stochastic simulation require a means to rapidly estimate inelastic responses for each sample of the simulation. Over the years, various approaches have been explored for the simulation of the inelastic response of wind excited systems [15, 16, 6, 17, 18, 7, 19, 20, 21, 22, 11, 23, 24, 25, 12]. To overcome the computational challenges stemming from the long duration of typical windstorms, which significantly hinder the application of existing methods based on direct integration, e.g., incremental dynamic analysis and is variants [26], as well as the need to capture failure mechanisms associated with accumulation of damage, which rule out the possibility of using approaches based on nonlinear static pushover analysis [27], the framework presented in [12] uses recently developed concepts rooted in the theory of plasticity [21, 22, 12]. In particular, based on the dynamic shakedown theory, this approach allows not only rapid identification of the safety against potential failure mechanisms of interest to wind engineering, e.g., low cycle fatigue and ratcheting, but also direct estimation of inelastic deformations occurring at shakedown. Despite the completeness and efficiency of this approach, it does not provide the time history

responses that are vital for directly estimating the hysteretic behavior of the system as well as the evolution of the inelastic deformations over the duration of the event. In addition, all inelastic response quantities are estimated at dynamic shakedown. As dynamic shakedown is an asymptotic behavior of the system after infinite repetition of the loading, the inelastic response quantities are in general greater than those actually occurring during a windstorm. This can lead to overly conservative estimates of reliability. Furthermore, this approach can only provide inelastic deformations if the structure is capable of reaching the state of dynamic shakedown. For samples for which dynamic shakedown is not achieved, such information remains unknown. Importantly, since the state of dynamic shakedown generally involves only a limited amount of inelasticity, this limitation hinders the application of the approach to collapse assessment where large inelastic deformations are expected. To address these issues, an alternative approach is required for efficiently estimating the inelastic response of wind excited structures within the setting of dynamic shakedown.

As an efficient alternative to classic direct integration methods, fast nonlinear analysis (FNA) was developed for rapidly carrying out nonlinear time history analysis where nonlinear behavior is restricted to a small number of predefined locations within a structure [28]. This approach solves the nonlinear system through a set of modal equations by treating nonlinear forces as external loads. This greatly improves the computational efficiency as compared to classic direct integration methods. Similar to direct integration methods, this approach provides a full range of global and local time history responses. The major limitation of the approach is the need to know a priori which structural members will experience inelasticity. This practically limits the approach to the time history analysis of structural systems that are equipped with nonlinear energy dissipation devices (components that are expected to respond with inelastic behavior while the rest of the structure remains elastic). To extend such an approach to structures without prior knowledge of the locations and extent of inelastic elements, an adaptive fast nonlinear analysis (AFNA) is proposed in this paper. The scheme is developed within the setting of stress resultant dynamic shakedown therefore enabling the benefits of shakedown analysis, i.e., the direct assessment of potential failure due to low cycle fatigue and ratcheting, to be integrated with the benefits afforded by direct integration schemes, i.e., knowledge of the evolution of inelasticity over the duration of the wind event

and beyond the state of dynamic shakedown. Finally, the scheme is integrated into the reliability assessment framework recently proposed in [12] therefore defining a framework that is capable of rapidly providing not only comprehensive inelastic time history information, but also reliability estimates for a full range of limit states, including incipient collapse.

2. The stress resultant setting and dynamic shakedown

2.1. The stress resultant setting and elastic solution

To model plasticity distributed along beam-column elements, a displacement-based formulation is adopted in this work. The displacement fields of the i_e th element of the structure $\mathbf{v}_{i_e}(x) = \{v_x(x), v_y(x), v_z(x)\}^{\mathrm{T}}$ are discretized and interpolated in terms of element end displacements \mathbf{u}_{i_e} through the following equation:

$$\mathbf{v}_{i_e}(x) = \mathbf{N}_{i_e}(x)\mathbf{u}_{i_e} \tag{1}$$

where $\mathbf{N}_{i_e}(x)$ is a matrix containing interpolation functions for the displacement fields for the i_e th element. Based on the assumption of Euler-Bernoulli beam theory, the associated deformation fields of the element, $\mathbf{d}_{i_e}(x)$, can be expressed as:

$$\mathbf{d}_{i_e}(x) = \{\epsilon_x(x), \kappa_y(x), \kappa_z(x)\}^{\mathrm{T}}$$

$$= \left\{ \frac{\partial v_x(x)}{\partial x}, \frac{\partial^2 v_y(x)}{\partial x^2}, -\frac{\partial^2 v_z(x)}{\partial x^2} \right\}^{\mathrm{T}}$$
(2)

where ϵ_x , κ_y and κ_z are the axial deformation and curvatures in the local x, y and z coordinate system for the i_e th element, which can be expressed in terms of element end displacements as:

$$\mathbf{d}_{i_e}(x) = \mathbf{B}_{i_e}(x)\mathbf{u}_{i_e} \tag{3}$$

with $\mathbf{B}_{i_e}(x)$ the strain-deformation matrix containing the first and second derivatives of the displacement interpolation functions. The internal forces at each section along the i_e th element $\mathbf{D}_{i_e}(x)$, including axial force $N_x(x)$ and bending moments $M_y(x)$ and $M_z(x)$, can be described by the following constitutive relation:

$$\mathbf{D}_{i_e}(x) = \{N_x(x), M_y(x), M_z(x)\}^{\mathrm{T}}$$

$$= \mathbf{k}_{s, i_e}(x)\mathbf{d}_{i_e}(x)$$
(4)

where $\mathbf{k}_{s,i_e}(x)$ is the section stiffness matrix. Based on the principle of virtual displacements, the element end forces can be related to the section forces through the equilibrium condition:

$$\mathbf{q}_{i_e} = \int_0^{L_{i_e}} \mathbf{B}_{i_e}^{\mathrm{T}}(x) \mathbf{D}_{i_e}(x) dx \tag{5}$$

where L_{i_e} is the length of the i_e th element. Replacing $\mathbf{d}_{i_e}(x)$ with Eq. (3) in the constitutive relation of Eq. (4), the linearization of Eq. (5) with respect to the element end displacements gives the element stiffness matrix \mathbf{k}_{i_e} :

$$\mathbf{k}_{i_e} = \frac{\partial \mathbf{q}_{i_e}}{\partial \mathbf{u}_{i_e}} = \int_0^{L_{i_e}} \mathbf{B}_{i_e}^{\mathrm{T}}(x) \mathbf{k}_{s,i_e}(x) \mathbf{B}_{i_e}(x) dx$$
 (6)

It should be observed that the distributed plasticity setting outlined above does not explicitly contemplate the modeling of plastic hinges which can complicate the modeling of certain types of problems involving inelasticity, e.g., progressive collapse.

Given the mechanical model described above, the dynamic equilibrium of a structural system with N degrees of freedom (DOF) subject to stochastic excitation can be written as:

$$\mathbf{M}\ddot{\mathbf{X}}(t) + \mathbf{C}\dot{\mathbf{X}}(t) + \mathbf{K}\mathbf{X}(t) = \mathbf{F}(t)$$
(7)

where $\mathbf{X}(t)$, $\dot{\mathbf{X}}(t)$, and $\ddot{\mathbf{X}}(t)$ are the $N \times 1$ dimensional vectors of the displacement, velocity, and acceleration responses in global coordinates, $\mathbf{F}(t)$ is the $N \times 1$ dimensional vector of stochastic excitation, while \mathbf{M} , \mathbf{C} , and \mathbf{K} are the $N \times N$ dimensional mass, damping, and elastic stiffness matrices of the system. The stiffness matrix \mathbf{K} can be determined by assembling the element stiffness matrix of Eq. (6) over the entire structure. The displacement response $\mathbf{X}(t)$ can be solved efficiently through a set of uncoupled equations using the modal approach, as follows:

$$\mathbf{\Theta}\ddot{\mathbf{Y}}(t) + \mathbf{\Lambda}\dot{\mathbf{Y}}(t) + \mathbf{\Omega}\mathbf{Y}(t) = \mathbf{\Phi}^{\mathrm{T}}\mathbf{F}(t)$$
(8)

where $\mathbf{\Phi} = [\boldsymbol{\phi}_1, \dots, \boldsymbol{\phi}_N]$ is a matrix containing the N stiffness normalized mode shapes (normalization with respect to stiffness is carried out as it avoids the numerical issues that can arise when treating DOF with zero mass), $\mathbf{Y}(t) = \{Y_1(t), \dots, Y_N(t)\}^T$, $\dot{\mathbf{Y}}(t) = \{\dot{Y}_1(t), \dots, \dot{Y}_N(t)\}^T$, and $\ddot{\mathbf{Y}}(t) = \{\ddot{Y}_1(t), \dots, \ddot{Y}_N(t)\}^T$ are vectors of the modal displacement, velocity, and acceleration responses, while $\mathbf{\Theta}$, $\mathbf{\Lambda}$, and $\mathbf{\Omega}$ are the generalized mass, damping,

and stiffness matrices calculated as:

$$\Theta = \Phi^{T} M \Phi, \quad \Lambda = \Phi^{T} C \Phi, \quad \Omega = \Phi^{T} K \Phi$$
(9)

It is worth noting that, in this formulation, the N modes of the system can be divided into dynamic modes, with non-zero masses, and quasi-static modes corresponding to the massless DOF. For the dynamic modes, the corresponding terms within the generalized damping matrix Λ are $2\xi_l/\omega_l$ in which ξ_l and ω_l are the lth modal damping ratio and circular frequency while the terms in the generalized mass matrix Θ are ω_l^{-2} with $\omega_l \to \infty$ for static modes. By solving the uncoupled Eq. (8), the response of the system can now be expressed by transforming the modal responses back to the physical coordinates as:

$$\mathbf{X}(t) = \mathbf{\Phi}\mathbf{Y}(t), \quad \dot{\mathbf{X}}(t) = \mathbf{\Phi}\dot{\mathbf{Y}}(t), \quad \ddot{\mathbf{X}}(t) = \mathbf{\Phi}\ddot{\mathbf{Y}}(t) \tag{10}$$

2.2. Stress resultant dynamic shakedown

For an external dynamic load that is periodic and of infinite duration, $\mathbf{F}_{\infty}(t)$, a necessary and sufficient condition for dynamic shakedown of an elastic-perfectly plastic (EPP) structural system discretized into $n_{\rm e}$ elements, is that there exists time-independent generalized self-stress, $\mathbf{D}_{i_{\rm e}}^{r}(x)$, such that the following condition holds for each integration point, x_{i} , of each element of the discretization [29]:

$$\mathbf{N}_{i_{e}}(x_{i})^{\mathrm{T}} \left(\mathbf{D}_{E,i_{e}}^{e}(t;x_{i}) + \mathbf{D}_{i_{e}}^{r}(x_{i}) \right) - \mathbf{R}_{i_{e}}(x_{i}) \le \mathbf{0} \quad x_{i} \in [0, L_{i_{e}}]$$
(11)

where L_{i_e} is the length of the i_e element, $\mathbf{R}_{i_e}(x_i)$ is the plastic resistance vector defined from the linearization of the stress-resultant yield domains associated with each integration point of the discretization, $\mathbf{N}_{i_e}(x_i)$ is the matrix that collects the unit external normals associated with each surface of the linearized yield domains, and $\mathbf{D}_{E,i_e}^s(t;x_i)$ is the steady-state elastic generalized stress vector.

The above condition requires the definition of $\mathbf{F}_{\infty}(t)$. Without loss of generality, $\mathbf{F}_{\infty}(t)$ can be defined from $\mathbf{F}(t)$ by simply considering $\mathbf{F}(t)$ repeated indefinitely:

$$\mathbf{F}_{\infty}(t + kT) = \mathbf{F}(t) \text{ for } k = 0, 1, ..., +\infty \text{ and } t \in [0, T)$$
 (12)

where T is the original duration of $\mathbf{F}(t)$. It should be noted that, as discussed in [21], no restrictions are placed on $\mathbf{F}(t)$ which can represent realizations of both stationary or non-stationary stochastic excitation. In particular, if it is assumed that $\mathbf{F}(t) = \mathbf{0}$ for t = 0 and a

period of calm is considered before each repetition of $\mathbf{F}(t)$, then the elastic response of the structure can be considered steady-state from t = 0 and $\mathbf{D}_{E,i_e}^s(t;x_i)$ can be obtained from Eqs. (3) and (4) as:

$$\mathbf{D}_{E,i_{\mathrm{e}}}^{s}(t;x_{i}) = \mathbf{k}_{\mathrm{s},i_{\mathrm{e}}}(x)\mathbf{B}_{\mathrm{s},i_{\mathrm{e}}}(x)\mathbf{u}_{\mathrm{e}}(t)$$
(13)

In general, to use Eq. (11) to check for the achievement of the state of dynamic shakedown, it is convenient to introduce a load multiplier s of \mathbf{F}_{∞} . The satisfaction of the dynamic shakedown condition of Eq. (11), can then be evaluated by solving the following linear programming problem [18, 7, 21]:

$$s_{p} = \max_{s, \mathbf{D}^{r}} s$$
subject to
$$\hat{\mathbf{D}}_{E}^{s} = \max_{t \in [0, T]} \mathbf{D}_{E}^{s}(t)$$

$$\mathbf{N}^{T} (s\hat{\mathbf{D}}_{E}^{s} + \mathbf{D}^{r}) - \mathbf{R} \leq \mathbf{0}$$
(14)

where \mathbf{D}^r is the vector collecting the generalized self-stresses at all integration points of the discretization; $\mathbf{D}_E^s(t)$ is the vector collecting the associated steady-state elastic generalized stress responses; and \mathbf{R} and \mathbf{N} are respectively the vectors of plastic resistances associated with the linearized yield domains and the block diagonal matrix collecting the unit external normals to the linearized yield domains all integration points. In addition, when solving Eq. (14), \mathbf{D}^r is expected to define a residual stress state that is self-balanced.

A similar linear programming problem can be defined for solving the elastic multiplier, s_e , i.e., the load multiplier beyond which nonlinearity will occur. To obtained s_e , \mathbf{D}^r in Eq. (14) is set to zero. It is important to note that, because high-dimensional linear programming problems can, in general, be very efficiently solved, evaluating s_e and s_p does not generally pose a computationally challenging problem. The multipliers s_e and s_p convey plenty of useful information on structural safety. For instance, s_p/s_e expresses the plastic reserve, i.e., the safety margin beyond the system-level first yield [12] before shakedown will no longer occur and the system becomes potentially susceptible to failure due to low-cycle fatigue and ratcheting. In addition, $s_e \geq 1$ indicates the structure will remain elastic under a given load and therefore responses estimated through the modal integration, i.e., by solving Eq. (8), are accurate. For samples with $s_e < 1$, however, nonlinear analyses will, in general, be

required. The strain-based schemes outlined in [21, 22, 12], serve this need with, however, the limitations discussed in Sec. 1. In the following, a step-by-step integration scheme will be developed that overcome these limitations and that can be naturally integrated within the dynamic shakedown setting outlined above.

3. Proposed adaptive fast nonlinear analysis (AFNA)

3.1. Problem setting

The AFNA approach developed in this work is based on the FNA schemes that were developed for rapid time history analysis of a special class of nonlinear system (i.e., systems with predefined locations of inelasticity) [28]. The FNA approach satisfies the fundamental equations of mechanics, including equilibrium, force-deformation, and compatibility. The exact force equilibrium of an inelastic system can be expressed by the following equations of motion:

$$\mathbf{M}\ddot{\mathbf{X}}(t) + \mathbf{C}\dot{\mathbf{X}}(t) + \mathbf{F}_{NL}(\dot{\mathbf{X}}, \mathbf{X}; t) = \mathbf{F}(t)$$
(15)

where $\mathbf{F}_{\rm NL}(\dot{\mathbf{X}}, \mathbf{X}; t)$ is a vector of nonlinear forces. By treating the nonlinear force as an external force and introducing the elastic stiffness matrix \mathbf{K} , Eq. (15) can be rewritten in a form similar to the linear elastic system, as follows:

$$\mathbf{M}\ddot{\mathbf{X}}(t) + \mathbf{C}\dot{\mathbf{X}}(t) + \mathbf{K}\mathbf{X}(t) = \mathbf{F}(t) - \mathbf{F}_{\text{NLC}}(\dot{\mathbf{X}}, \mathbf{X}; t)$$
(16)

where $\mathbf{F}_{\mathrm{NLC}}(\dot{\mathbf{X}}, \mathbf{X}; t) = \mathbf{F}_{\mathrm{NL}}(\dot{\mathbf{X}}, \mathbf{X}; t) - \mathbf{K}\mathbf{X}(t)$ is the nonlinear correction force. Eq. (16) can then be solved in the modal space as:

$$\mathbf{\Theta}\ddot{\mathbf{Y}}(t) + \mathbf{\Lambda}\dot{\mathbf{Y}}(t) + \mathbf{\Omega}\mathbf{Y}(t) = \mathbf{\Phi}^{\mathrm{T}}\left[\mathbf{F}(t) - \mathbf{F}_{\mathrm{NLC}}(\dot{\mathbf{Y}}, \mathbf{Y}; t)\right]$$
(17)

Through mode truncation, this formulation greatly reduces the size of the nonlinear system to be solved. However, unlike the elastic form of Eq. (8), Eq. (17) is not uncoupled because of the existence of the nonlinear force vector $\mathbf{F}_{NLC}(\dot{\mathbf{Y}}, \mathbf{Y}; t)$. Hence, it must be solved for all required modes simultaneously. To improve the efficiency of nonlinear time history analysis, a piece-wise exact method can be used to solve the modal responses iteratively at each time

instant t with initial values determined from the following Taylor series expansion:

$$\begin{cases} \mathbf{Y}(t+\Delta t) = \mathbf{Y}(t) + \dot{\mathbf{Y}}(t)\Delta t + 0.5\ddot{\mathbf{Y}}(t)\Delta t^2 + \mathcal{O}(\Delta t^3) \\ \dot{\mathbf{Y}}(t+\Delta t) = \dot{\mathbf{Y}}(t) + \ddot{\mathbf{Y}}(t)\Delta t + \mathcal{O}(\Delta t^2) \end{cases}$$
(18)

where Δt is the time step considered in the analysis and \mathcal{O} is the big O notation that refers to the infinitesimal functions of the same order. In particular, by first identifying the locations of nonlinear elements in the structure, the iterative process within each time step is only carried out for those predefined locations. This results in a significant reduction in computational efforts and therefore computer time required to obtain a solution. However, the requirement to identify a priori the locations of the nonlinear elements is a major limitation as in general it is not possible to know where nonlinearity may occur in the system.

3.2. The proposed stress resultant adaptive solution process

Based on the mechanical model of Sec. 2.1 and the FNA approach described in Sec. 3.1, an adaptive scheme is defined in this work to efficiently estimate the inelastic response histories. The key feature of the proposed approach is the capability to update, at each time step, the potential nonlinear locations, time step sizes, and the number of modes to be considered in the analysis. In particular, the scheme is based on the possibility of rapidly evaluating the section deformations that characterize the nonlinearity of the structure at each integration point. To this end, it is first convenient to introduce the section deformation – modal coordinate transformation matrix, Ψ_l , where each column of the matrix, Ψ_l with l = 1, ..., N, represents the section deformations, i.e., axial strains and curvatures, at all integration points of the discretization due to a unit modal displacement at mode l, as follows:

$$\Psi = \mathbf{B}\mathbf{T}\Phi \tag{19}$$

in which $\mathbf{T} = \operatorname{diag}[\mathbf{T}_1, \dots, \mathbf{T}_{i_e}, \dots, \mathbf{T}_{n_e}]$ is a block diagonal matrix collecting the global to local coordinate transformation matrices, \mathbf{T}_{i_e} , for all n_e elements of the discretization, while $\mathbf{B} = \operatorname{diag}[\mathbf{B}_1, \dots, \mathbf{B}_{i_e}, \dots, \mathbf{B}_{n_e}]$ is a block diagonal matrix collecting the strain-deformation matrices, \mathbf{B}_{i_e} , for all n_e elements, where $\mathbf{B}_{i_e} = [\mathbf{B}_{i_e}^{\mathrm{T}}(x_1), \mathbf{B}_{i_e}^{\mathrm{T}}(x_2), \dots, \mathbf{B}_{i_e}^{\mathrm{T}}(x_{n_s})]^{\mathrm{T}}$ consists of the strain-deformation matrices for all n_s integration points along the i_e th element.

3.2.1. Elastic solver with large time step

In a given time step, the solution process first solves for the elastic responses considering a time step Δt . The elastic solution is estimated through modal analysis while considering the first m_d dynamically significant modes as well as an additional m_b modes for which the background response, or quasi-static response, is estimated. A piece-wise exact method is adopted in calculating the modal response time histories [28, 31]. The corresponding responses at the section level (local state) can then be determined as:

$$\begin{cases} \mathbf{d}(t + \Delta t) = \bar{\mathbf{\Psi}}(\bar{\mathbf{Y}}(t + \Delta t) - \bar{\mathbf{Y}}(t)) + \mathbf{d}(t) \\ \dot{\mathbf{d}}(t + \Delta t) = \bar{\mathbf{\Psi}}(\dot{\bar{\mathbf{Y}}}(t + \Delta t) - \dot{\bar{\mathbf{Y}}}(t)) + \dot{\mathbf{d}}(t) \end{cases}$$
(20)

where $\mathbf{d} = \{\mathbf{d}_1, \dots, \mathbf{d}_{n_e \times n_s}\}^{\mathrm{T}}$ is a vector of section deformations for all integration points of all elements of the discretization while $\dot{\mathbf{d}}$ represents the rate of change of \mathbf{d} ; $\bar{\mathbf{\Psi}}$, $\bar{\mathbf{Y}}$, and $\dot{\mathbf{Y}}$ are respectively truncated versions of $\mathbf{\Psi}$, \mathbf{Y} , and $\dot{\mathbf{Y}}$, with terms related to the first $\bar{m} = m_d + m_b$ modes. The elastic predictor of the section forces can then be determined and checked against the yielding criteria using the linear elastic section constitutive relation of Eq. (4) for all sections, i.e., $\mathbf{D}_E(t+\Delta t) = \mathbf{K}_s\mathbf{d}(t+\Delta t)$ where $\mathbf{K}_s = \mathrm{diag}[\mathbf{k}_{s_1}, \dots, \mathbf{k}_{s_{n_e \times n_s}}]$ is the block diagonal matrix containing the section stiffness matrices \mathbf{k}_s for all integration points of the discretization. The solution process moves on to the next time step only if the sum of the elastic forces and the nonlinear correction forces for all integration points remain within the yield domain, i.e., the structure remains elastic or is in the linear unloading/reloading stage, as follows:

$$\mathbf{N}^{\mathrm{T}} \left(\mathbf{D}_{E}(t + \Delta t) + \mathbf{D}_{\mathrm{NLC}}(t) \right) - \mathbf{R} \le \mathbf{0}$$
 (21)

where $\mathbf{D}_{\mathrm{NLC}}(t)$ is the nonlinear section correction forces of the previous time step:

$$\mathbf{D}_{\mathrm{NLC}}(t) = \mathbf{D}(t) - \mathbf{D}_{E}(t) = \mathbf{D}(t) - \mathbf{K}_{\mathrm{s}}\mathbf{d}(t)$$
(22)

in which $\mathbf{D}(t)$ is the vector of section forces determined from the inelastic constitutive law.

At this juncture, it is important to observe that the dynamic shakedown problem of Sec. 2.2 is based on the assumption, at the level of the stress resultants, of an EPP material behavior and associated flow rule. Under this assumption, the nonlinear correction forces of Eq. (22) are constant when the structure is in an elastic unloading/reloading stage, i.e., they do not need updating when the structure is responding elastically.

If the condition of Eq. (21) is not met, i.e., inelasticity occurs, the solution process moves back to the previous step and begins an adaptive solution process with a reduced step size $\Delta t/\eta$, where $\eta \in \mathbb{Z}^+$ is a step size modifier, to estimate the corresponding nonlinear section correction force, $\mathbf{D}_{\mathrm{NLC}}(t + \Delta t/\eta)$. It should be noted that the piece-wise exact method assumes the change in $\mathbf{\Phi}^{\mathrm{T}}[\mathbf{F}(t) - \mathbf{F}_{NLC}(\dot{\mathbf{Y}}, \mathbf{Y}; t)])$ within each time step to be linear. While for $\mathbf{F}(t)$ the adequacy of this assumption is related to choosing an appropriate sampling frequency, for $\mathbf{F}_{NLC}(\dot{\mathbf{Y}}, \mathbf{Y}; t)$ the adequacy of the assumption is related to the period T_{\min} , i.e., the shortest period of the m_d retained dynamic modes. Numerically, a value of $T_{\min}/2$ is a natural limit as it ensures at least two points to characterize the variation of $\mathbf{F}_{NLC}(\dot{\mathbf{Y}}, \mathbf{Y}; t)$ over T_{\min} . Nevertheless, to ensure the best balance between accuracy and numerical efficiency, the modified time step $\Delta t/\eta$ should be taken to be less than or equal to $T_{\min}/4$, where T_{\min} is the smallest period associated with the m_d dynamic modes.

3.2.2. The adaptive solver

Initial step. In the adaptive process, the modal responses for the adjusted reduced time step, i.e., $\bar{\mathbf{Y}}(t + \Delta t/\eta)$ and $\dot{\bar{\mathbf{Y}}}(t + \Delta t/\eta)$ are first estimated for the first \bar{m} modes by the Taylor series expansion of Eq. (18). The corresponding section forces are once again determined based on the section constitutive relation of Eq. (4). The locations of the nonlinearity in the structural system can then be determined by the following criterion:

$$\mathbf{N}^{\mathrm{T}}(\mathbf{D}_{E}(t + \Delta t/\eta) + \mathbf{D}_{\mathrm{NLC}}(t)) - \nu \mathbf{R} \ge \mathbf{0}$$
(23)

where $\nu \in [0, 1]$ is a scaling factor used to ensure the number of elements identified as potentially inelastic is not unduly affected by the approximations inherent to the Taylor series expansion of Eq. (18). A smaller value of ν should be used if a more conservative estimate of potential locations of nonlinearity is desired. If no sections (integration points) meet the criterion of Eq. (23), the responses at the current time step will be solved directly through the piece-wise exact method. The solution process then proceeds to the next reduced time step, $t+2\Delta t/\eta$, and reevaluates Eq. (23). If there is any section identified as a potential nonlinear location, i.e., any section satisfying Eq. (23), the following iterative approach will be adopted to evaluate the nonlinear responses.

The iterative process. The iterative process, indexed k, commences from a first estimate of the complete modal response, $\mathbf{Y}^{(k)}(t+\Delta t/\eta)$ and $\dot{\mathbf{Y}}^{(k)}(t+\Delta t/\eta)$, estimated by appending to $\bar{\mathbf{Y}}(t+\Delta t/\eta)$ and $\dot{\mathbf{Y}}(t+\Delta t/\eta)$ the last computed values of the responses of the additional $(N-\bar{m})$ modes, $\mathbf{Y}_{(N-\bar{m})}$ and $\dot{\mathbf{Y}}_{(N-\bar{m})}$. In particular, if the system is experiencing inelasticity for the first time, $\mathbf{Y}_{(N-\bar{m})}$ and $\dot{\mathbf{Y}}_{(N-\bar{m})}$ are simply taken as zero. From the full modal response and by considering only the potential nonlinear sections identified from Eq. (23), the local states, i.e., the section deformations, for the current iteration can be determined as:

$$\begin{cases} \tilde{\mathbf{d}}^{(k)}(t + \Delta t/\eta) = \tilde{\mathbf{\Psi}}\mathbf{Y}^{(k)}(t + \Delta t/\eta) \\ \dot{\tilde{\mathbf{d}}}^{(k)}(t + \Delta t/\eta) = \tilde{\mathbf{\Psi}}\dot{\mathbf{Y}}^{(k)}(t + \Delta t/\eta) \end{cases}$$
(24)

where $\tilde{\mathbf{d}}(t + \Delta t/\eta)$, $\dot{\tilde{\mathbf{d}}}(t + \Delta t/\eta)$, and $\tilde{\mathbf{\Psi}}$ are respectively the subsets of $\mathbf{d}(t + \Delta t/\eta)$, $\dot{\mathbf{d}}(t + \Delta t/\eta)$, and $\mathbf{\Psi}$ containing only relevant rows for the identified nonlinear sections (for the remainder of this section, the accent \sim indicates consideration of the subset of integration points with identified inelasticity). Based on the responses calculated from Eq. (24) and the corresponding response increments with respect to the previous time step, the nonlinear section force increments $\Delta \tilde{\mathbf{D}}^{(k)}(t + \Delta t/\eta)$, can be estimated from the mechanical properties and deformation history of each nonlinear section. The associated increment in the correction forces can then be evaluated as:

$$\Delta \tilde{\mathbf{D}}_{\mathrm{NLC}}^{(k)}(t + \Delta t/\eta) = \Delta \tilde{\mathbf{D}}^{(k)}(t + \Delta t/\eta) - \tilde{\mathbf{K}}_s \Delta \tilde{\mathbf{d}}^{(k)}(t + \Delta t/\eta)$$
 (25)

where $\Delta \tilde{\mathbf{d}}^{(k)}(t + \Delta t/\eta)$ is the increment of $\tilde{\mathbf{d}}^{(k)}(t + \Delta t/\eta)$ at the current time step. Under the assumption of an EPP material and associated flow rule, the increment in nonlinear section correction forces, $\Delta \tilde{\mathbf{D}}_{\mathrm{NLC}}^{(k)}(t + \Delta t/\eta)$, can be efficiently identified through solving the following Haar-Kàrmàn condition:

$$\min_{\Delta \tilde{\mathbf{D}}_{\mathrm{NLC}}^{(k)}(t+\Delta t/\eta)} \frac{1}{2} \Delta \tilde{\mathbf{D}}_{\mathrm{NLC}}^{(k)}(t+\Delta t/\eta)^{\mathrm{T}} \tilde{\mathbf{K}}_{\mathrm{s}}^{-1} \Delta \tilde{\mathbf{D}}_{\mathrm{NLC}}^{(k)}(t+\Delta t/\eta)$$
subject to
$$\tilde{\mathbf{N}}^{\mathrm{T}} \left(\tilde{\mathbf{K}}_{\mathrm{s}} \tilde{\mathbf{d}}^{(k)}(t+\Delta t/\eta) + \tilde{\mathbf{D}}_{\mathrm{NLC}}^{(k)}(t+\Delta t/\eta) \right) - \tilde{\mathbf{R}} \leq \mathbf{0}$$
(26)

where $\tilde{\mathbf{D}}_{\mathrm{NLC}}^{(k)}(t+\Delta t/\eta) = \tilde{\mathbf{D}}_{\mathrm{NLC}}(t) + \Delta \tilde{\mathbf{D}}_{\mathrm{NLC}}^{(k)}(t+\Delta t/\eta)$. The use of the Haar-Kàrmàn condition for finding $\Delta \tilde{\mathbf{D}}_{\mathrm{NLC}}^{(k)}(t+\Delta t/\eta)$ can be traced back to how the problem of Eq. (26) is a quadratic

programming problem (QPP) that can be very efficiently solved by a number of standard QPP solvers without loss of generality. The corresponding increment in the nonlinear correction force vector can then be determined through the following transformation:

$$\Delta \mathbf{F}_{\mathrm{NLC}}^{(k)}(t + \Delta t/\eta) = \tilde{\mathbf{T}}^{\mathrm{T}} \Delta \tilde{\mathbf{q}}_{\mathrm{NLC}}^{(k)}(t + \Delta t/\eta)$$
(27)

where $\Delta \tilde{\mathbf{q}}_{\mathrm{NLC}}^{(k)}(t + \Delta t/\eta)$ is the vector collecting the increments in element end nonlinear correction forces determined by solving Eq. (5) through an appropriate integration scheme. The nonlinear correction forces are then updated as:

$$\mathbf{F}_{\mathrm{NLC}}^{(k+1)}(t + \Delta t/\eta) = \mathbf{F}_{\mathrm{NLC}}(t) + \Delta \mathbf{F}_{\mathrm{NLC}}^{(k)}(t + \Delta t/\eta) \tag{28}$$

The modal responses, $\mathbf{Y}^{(k+1)}(t+\Delta t/\eta)$ and $\dot{\mathbf{Y}}^{(k+1)}(t+\Delta t/\eta)$, can then be updated through the piece-wise exact method while considering all modes, i.e., now that the system is responding inelasticity, the number of modes considered in the solution process is increased from \bar{m} to N. In particular, the additional $(N-\bar{m})$ modes are assumed to respond in a quasi-static fashion therefore avoiding numerical instability.

Eq. (28) will be updated recursively until a user-defined convergence criterion is met. This can be defined in terms of any response parameter of interest, e.g., the difference in nonlinear correction forces, i.e., $|\mathbf{F}_{\text{NLC}}^{(k+1)} - \mathbf{F}_{\text{NLC}}^{(k)}| < e_{F_{NLC}}$ with $e_{F_{NLC}}$ a convergence tolerance.

3.3. Summary of the proposed AFNA scheme

The scheme commences by seeking to solve the system through elastic modal integration while considering the first \bar{m} modes, of which m_d are considered dynamic with the remaining m_b treated as quasi-static. At each time step, every integration point is checked for potential inelasticity. If inelasticity is identified at one or more integration points, the time step is reduced and the iterative process is invoked while considering not only the first \bar{m} modes but also all remaining $(N - \bar{m})$ modes that are treated as quasi-static. Once convergence of the iterative process is achieved, the solution process proceeds to the next time step and invokes the iterative process again if necessary, i.e., if Eq.(23) is not satisfied. The process ends once the time sequence of loading ends, providing a full range of inelastic response histories for structures modeled within the setting of the stress resultant dynamic shakedown problem of Sec.2.2. It should be observed that to account for P-Delta effects, a reduced stiffness matrix

is considered based on the linearized P-Delta model outlined in [33, 28]. The overall solution process is summarized in the flowchart of Fig. 1.

3.4. Validation

3.4.1. Preamble

In order to validate the proposed AFNA approach, it is applied to the inelastic response analysis of the steel structure of Fig. 2. In particular, the frame indicated in Fig. 2(a) is extracted and analyzed in two dimensions (2D). To validate, the results obtained from AFNA are compared to those obtained from direct integration carried out in OpenSees [34]. To enable this comparison, the extracted steel frame, illustrated in Fig. 2(b), was modeled using a fiber-based discretization as OpenSees does not have a stress resultant modeling environment. As such, the AFNA approach was reformulated at the fiber level.

3.4.2. Description

The building was assumed to be located in the Miami region of Florida, USA. As illustrated in Fig. 2(b), typical story heights are 6 m at ground level and 4 m for all other levels. The overall height of the building is 150 m. The moment resisting frame consists of wide flange standard W×24 beams with 5 m spans and square box columns. In particular, the dimension of the box column is defined by the centerline diameters, D, with thickness defined as D/20. Table 1 reports a summary of the section sizes. The steel composing the frame is assumed to follow an EPP constitutive law with an elastic modulus of 200 GPa and a yield stress of 355 MPa. The mass of the structure is estimated from its self-weight as well as a carried mass of 100 kg/m³. Material damping was modeled by Rayleigh damping calibrated to provide a damping ratio of 2.5% in the first two modes.

Fig. 3 illustrates the fiber discretization used for the sections of the beam and columns. To ensure consistency with the AFNA approach, the steel frame was modeled in OpenSees using displacement-based beam-column elements with 5-point Gauss-Legendre integration scheme. The nonlinear response in OpenSees was obtained using a dynamic updating analysis scheme based on the average constant acceleration Newmark-beta method. In particular, the Newton-Raphson (NR) algorithm with line search was first considered with a basic time step, Δt , of 0.02 s. If the solution failed to converge, the following series of algorithms were then

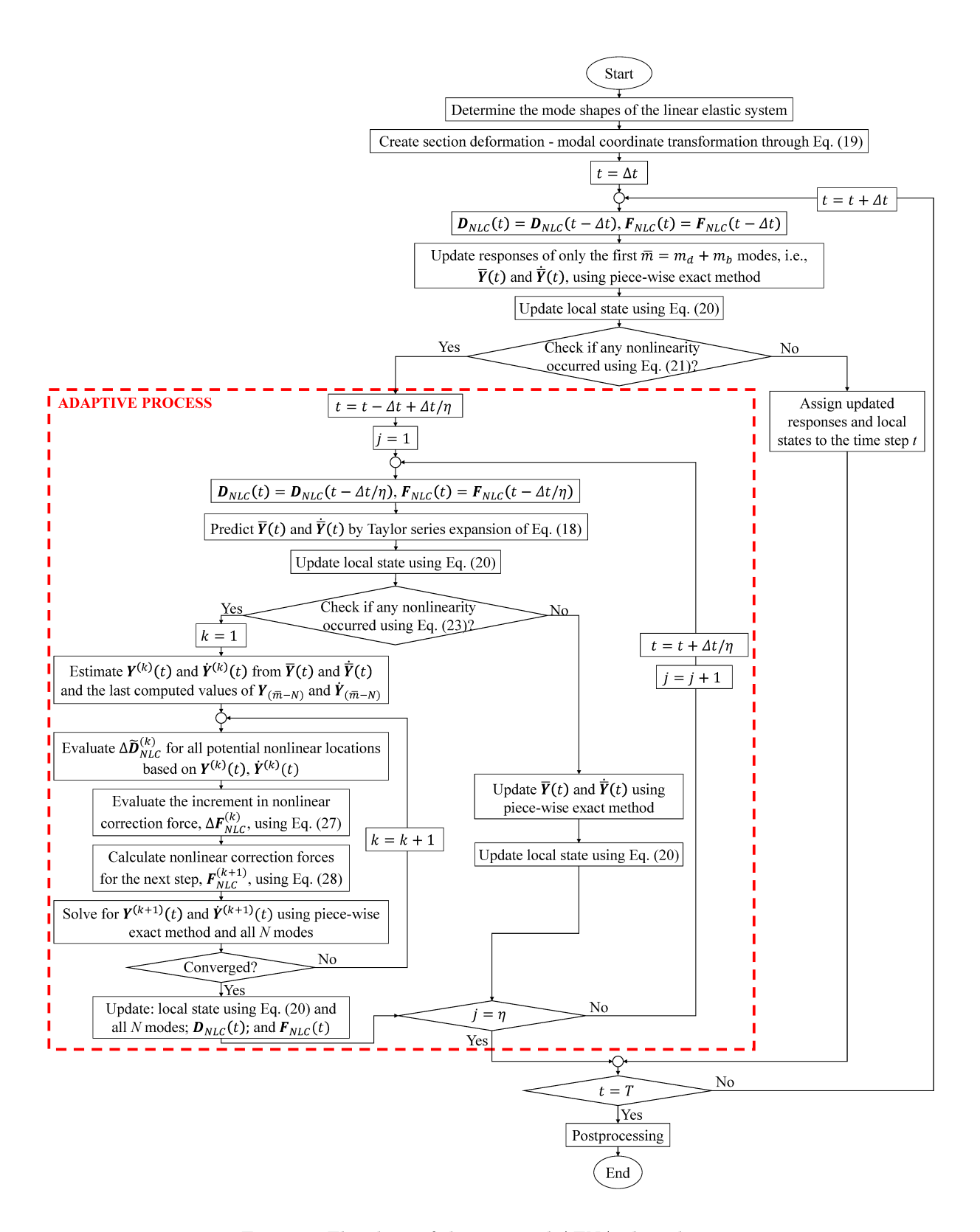


Figure 1: Flowchart of the proposed AFNA algorithm.

adopted sequentially until convergence was achieved: (1) modified NR algorithm with time step $\Delta t = 0.002$ s; (2) NR with line search algorithm and $\Delta t = 0.002$ s; (3) NR algorithm with $\Delta t = 0.001$ s; and (4) Broyden algorithm with $\Delta t = 0.001$ s. The convergence criteria were defined as achieving a norm of the displacement increment of 10^{-8} and an increment of total deformation energy of 10^{-10} . The first $m_d = 6$ dynamically significant modes, without additional $m_b = 0$ modes, were considered in the AFNA approach. The initial time step was taken as $\Delta t = 0.5$ s. In the adaptive process, the scaling factor, ν , was taken as 1.0. A time step modifier of $\eta = 3$ was considered. Maximum absolute increments in fiber strains of 10^{-6} were chosen as the convergence criteria.

Wind directions of $\alpha = 0^{\circ}$ and $\alpha = 90^{\circ}$ were considered, which, as can be seen from Fig. 2(a), correspond to acrosswind and alongwind loading. To ensure a high and similar level of nonlinearity, the mean wind speed at the building top, \bar{v}_y , was set to 70 m/s in the acrosswind direction and 65 m/s in the alongwind direction. The dynamic wind loads acting on the frame for the two wind directions were estimated as random realizations of the data-informed stochastic spectral proper orthogonal decomposition (POD) model outlined in [37, 21] (further details on this model are provided in Sec. 4.2.3). The model was calibrated to a wind tunnel data set obtained from the Tokyo Polytechnic University (TPU) aerodynamic database [38] for a building geometry consistent with Fig. 2. In particular, the data was collected on a 1/300 rigid model for a total recorded duration of 32 s using a sampling frequency of 1000 Hz and wind speed at the model top of 11 m/s. The loads acting on the 2D frame were estimated as 1/6 of the X-direction loads of the 3D building. The first five spectral POD modes were considered in simulating the load histories with a sampling frequency of 2 Hz. To ensure stability and accuracy when carrying out direct integration, wind loads between two successive sampling points were determined by linear interpolation. The total length of the wind storm was set to T = 600 s, in which the first and last minute were linearly ramped.

3.4.3. Results

Fig. 4 reports the time histories of the displacement responses at the three recorder levels indicated in Fig. 2(b). As can be seen, the two response time histories are almost identical,

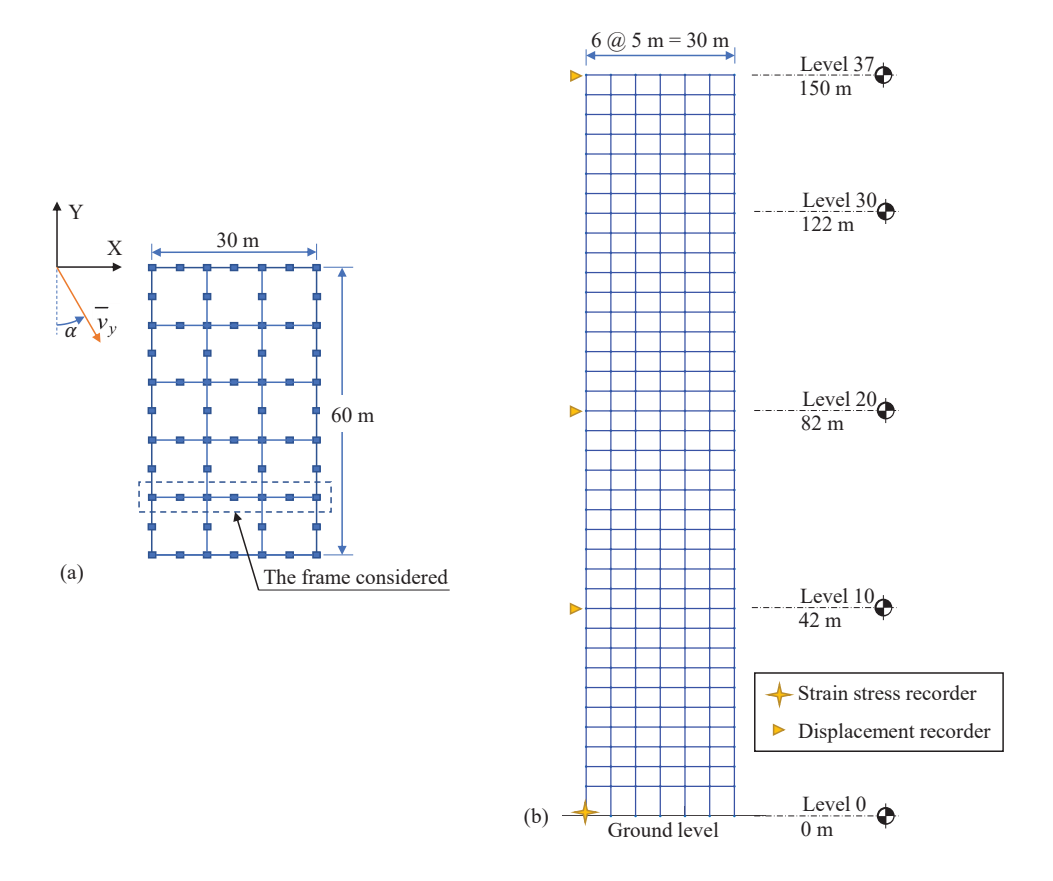


Figure 2: Schematic of the 37-story building: (a) Plan view of the building with the extracted 2D frame indicated; (b) illustration of the 2D frame.

Wide-flange Beams	Box Columns
Section size	Section size (m)
$W24 \times 192$	D = 0.5
$W24 \times 192$	D = 0.5
$W24\times103$	D = 0.4
$W24 \times 103$	D = 0.35
	Section size $W24 \times 192$ $W24 \times 192$ $W24 \times 103$

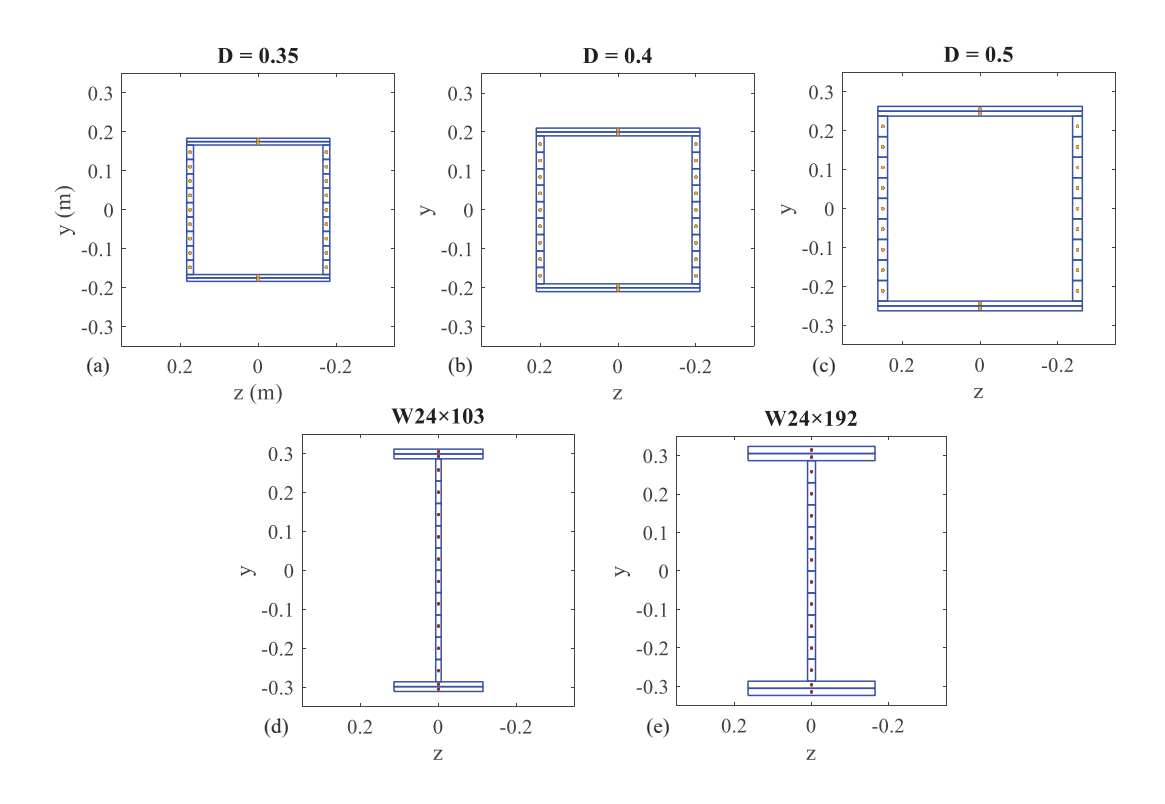


Figure 3: Fiber discretization of the: (a) Box column with D=0.35; (b) Box column with D=0.4m; (c) Box column with D=0.5; (d) W24×103 beam; and (e) W24×192 beam.

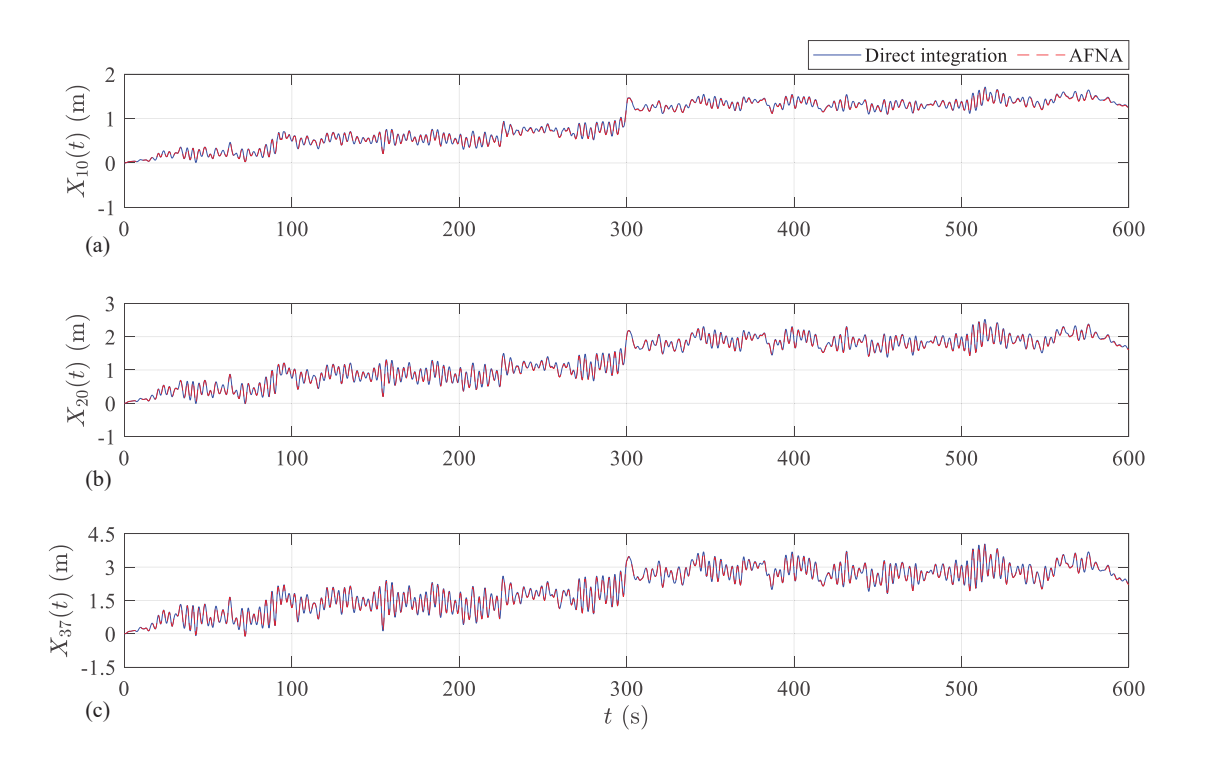


Figure 4: Comparison of the horizontal displacement response at the: (a) 10th; (b) 20th; and (c) 37th floors for alongwind loads.

demonstrating the accuracy of the proposed AFNA approach. The comparison between the stress and strain time histories, as well as the hysteretic curves, for alongwind loading is shown in Fig. 5 for the recorder indicated in Fig. 2(b). Similarly to the global response, it can be observed that the AFNA approach accurately reproduces the response of the system. The same level of accuracy is also seen for acrosswind loading, as shown in Figs. 6 and 7 that report the comparison between the displacement and fiber stress-strain responses.

While the comparison of this section was based on two randomly generated alongwind and acrosswind wind load histories, similar results were seen for a full suite of wind speeds, wind directions, and wind load realizations, therefore demonstrating the validity of the proposed AFNA approach.

4. Reliability Assessment Framework through AFNA

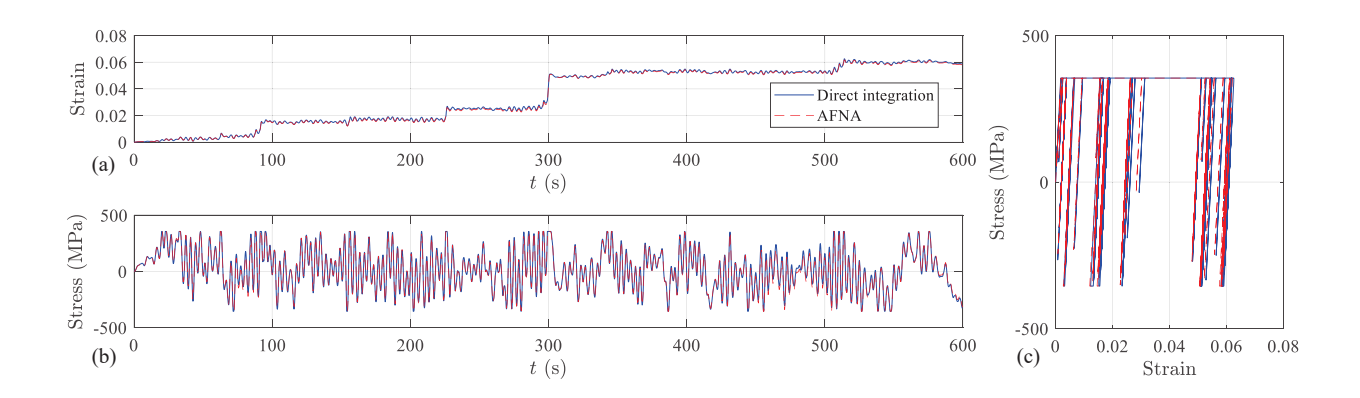


Figure 5: Fiber response comparison for a representative fiber of the exterior first-floor column and alongwind loads: (a) fiber strain; (b) fiber stress; and (c) hysteretic curve.

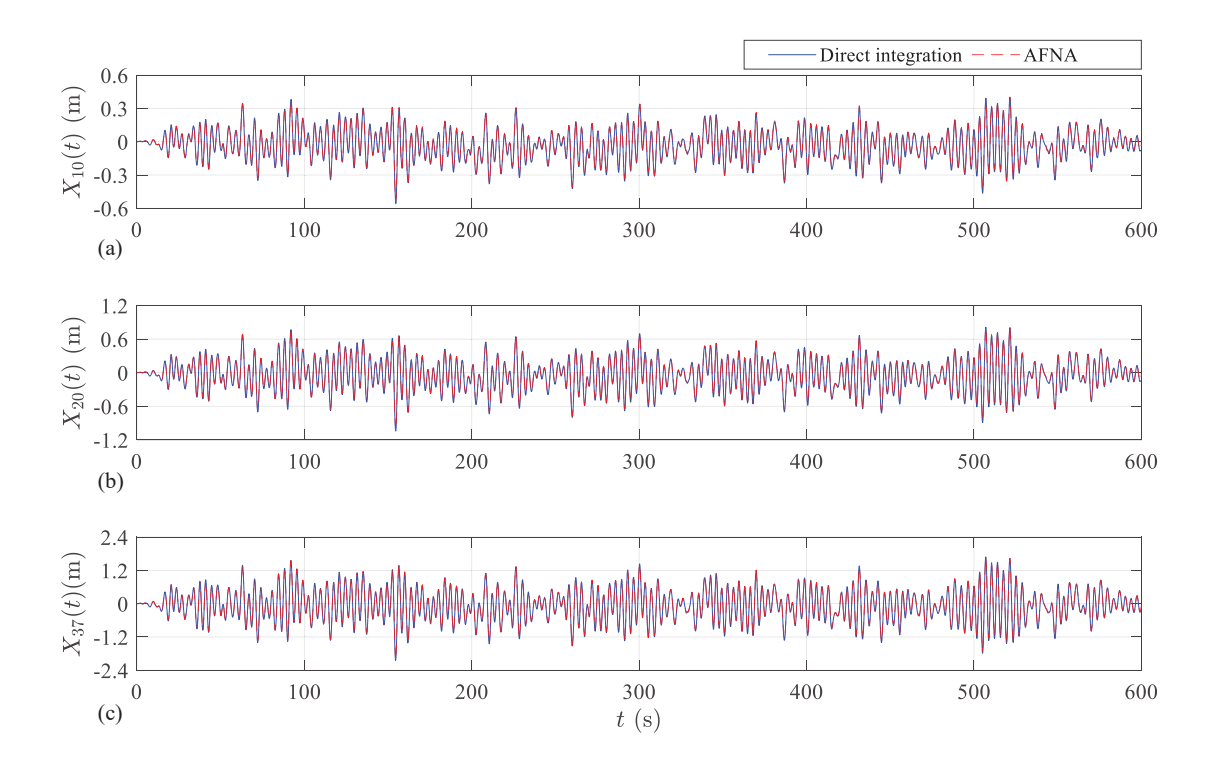


Figure 6: Comparison of the horizontal displacement response at the: (a) 10th; (b) 20th; and (c) 37th floors for acrosswind loads.

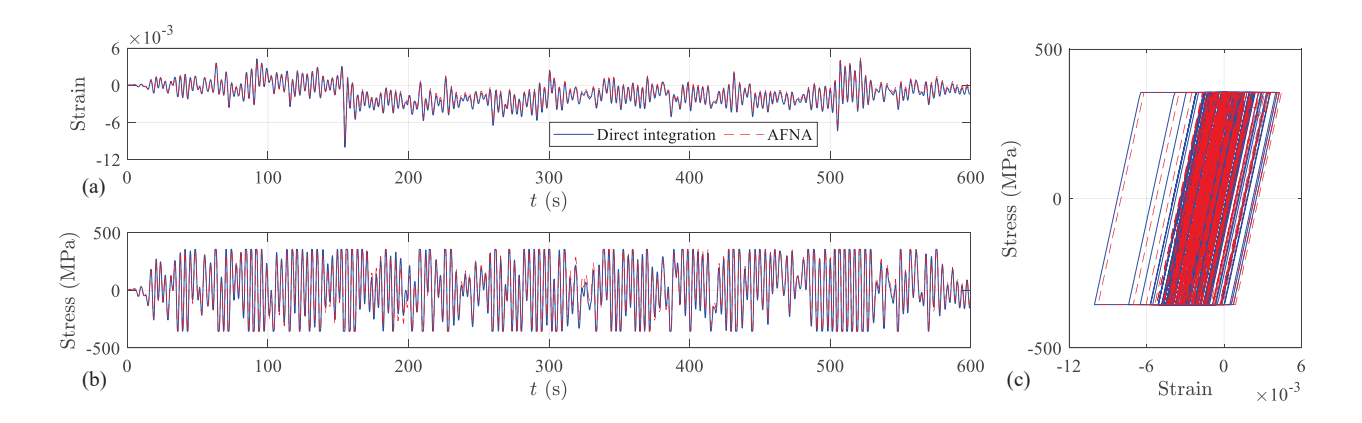


Figure 7: Fiber response comparison for a representative fiber of the exterior first-floor column and acrosswind loads: (a) fiber strain; (b) fiber stress; and (c) hysteretic curve.

4.1. Problem setting

The efficiency and accuracy in analyzing inelastic responses, together with the natural synergy with dynamic shakedown analysis, makes the AFNA scheme an ideal inelastic response simulator within the dynamic shakedown-based wind reliability analysis framework outlined in [12]. To this end, the reliability of a structure against a limit state of interest, described through a limit state function, g, that by convention assumes negative values when the limit state is violated, can be directly measured in terms of the probability of g assuming negative values and therefore as:

$$P_f = P(g(\mathbf{Z}) < 0) = \int \dots \int I[g(\mathbf{z})] f_{\mathbf{Z}}(\mathbf{z}) d\mathbf{z}$$
(29)

where \mathbf{Z} is a vector of random variables that include uncertainties in both the structural system and external loads; $f_{\mathbf{Z}}(\mathbf{z})$ is the joint probability density function of \mathbf{Z} ; and $I[g(\mathbf{Z})]$ is the indicator function which assumes the value of unity if failure occurs and zero otherwise. Based on the estimated value of P_f , the corresponding reliability index can be evaluated through the first-order reliability method (FORM) as:

$$\beta = \Phi^{-1}(1 - P_f) \tag{30}$$

where β is the reliability index associated with the limit state g = 0.

Concerning the limit state functions g, the following four classes of limit states are of interest [12]:

- 1. LS1: component-level yield (traditional limit state used in current design);
- 2. LS2: system-level first yield;
- 3. LS3: inability to achieve the state of dynamic shakedown;
- 4. LS4: inelastic displacement-based limit states.

In particular, as current codes and standards for wind are based on calibration to component-level first yield limit states, the class LS1 stands as a reference for ensuring design meet current code requirements. The classes LS2, LS3, and LS4 are consistent with the push towards explicit system-level evaluation of structural systems that are allowed to experience controlled inelasticity under extreme winds.

4.2. Model and load uncertainty

4.2.1. Overview

To ensure the reliabilities estimated through solving Eq. (30), and therefore Eq. (29), are meaningful from a design standpoint, it is important to consider a full range of code-consistent uncertainties. In general, these will include uncertainty in the model parameters, gravity loads, and wind loads. Based on the framework outlined in [12], the following sections will provide an overview of how these uncertainties are treated in this work.

4.2.2. Model and gravity load uncertainty

Of the model uncertainties, the mechanical properties of the materials are of primary importance. Within the stress resultant setting of this work, these include the yield strength and Young's modulus of steel members and the compressive strength of concrete and yield strength of the steel for reinforced concrete members. These basic random variables, can be used to completely characterize the uncertainty yield domains, \mathbf{R} , of the members composing the structural system. By observing how the stiffness of reinforced concrete members, can be directly related to the compressive strength of the concrete, they also define the uncertainty the structural stiffness \mathbf{K} . The systems of this work are dynamic and will therefore be affected by uncertainty in the damping. By taking advantage of the relationship of the proposed AFNA scheme with classic modal integration, a straightforward approach to model this uncertainty, and that will be followed in this work, is to take the damping ratios, ξ_l , of the generalized damping matrix of Eq. (9) as basic random variables.

The uncertainty in the gravity loads affects both the dead and live load. This uncertainty can be characterized through the probabilistic models outlined in [39, 40] that were developed explicitly for carrying out reliability analysis. In particular, as this work is focused on the reliability of systems subject to extreme winds, uncertain "arbitrary point-in-time" live loads should be considered for combination with the probabilistic dead loads and stochastic wind loads.

4.2.3. Wind load uncertainty

Wind load uncertainty must be defined at both the climatological and aerodynamic level. At the climatological level, the intensity of the wind event is generally characterized through the site-specific maximum mean hourly wind speed, v_H , at a reference height of H. To account for wind directionality, a sector-by-sector approach can be adopted in which the uncertainty in v_H is characterized for a specified number of wind sectors, typically 8 to 16 [41, 42]. Following this approach, the uncertainty in the largest wind speeds to occur over a life span of y years in wind sector s can be characterized through the following complementary cumulative distribution function (CCDF):

$$G_s(v_H) = 1 - [F_{V_H}(v_H|s)]^y$$
(31)

where $F_{V_H}(v_H|s)$ is the annual cumulative distribution function of v_H conditioned on wind blowing down sector s. The uncertainty in wind direction, α , within a given sector can be characterized in a similar manner and therefore through an appropriate CCDF, $G_s(\alpha|v_H)$.

At the aerodynamic level, for a given wind speed and direction pair, (v_H, α) , dynamic wind loads are required that capture record-to-record variability, i.e., stochasticity. As outlined in [37, 12], this can be achieved through the use of sotchastic wind load models that are based on calibrating a spectral proper orthogonal decomposition (POD) model to building specific wind tunnel data. In general, these data need to be collected using the synchronous multipressure sensing system technique as this allows for the direct estimation, through appropriate integration of the pressures, of the wind loads acting at each floor of the building. The use of building-specific wind tunnel data ensures the full capture of any complex aerodynamic features, e.g., vortex shedding and/or detached flow, seen in the wind tunnel. With this

model, the ith component of the stochastic wind load vector, $\mathbf{F}(t; v_H, \alpha)$, can be written as:

$$F_i(t; v_H, \alpha) = w_1 w_2 w_3 \sum_{l=1}^{N_l} \sum_{k=1}^{N_{k-1}} 2|\Upsilon_{il}(\omega_k; \alpha)| \sqrt{\chi_l(\omega_k; v_H, \alpha) \Delta \omega} \cos(\omega_k t + \theta_{il}(\omega_k; \alpha) + \hat{\theta}_{lk})$$
(32)

where: Υ_{il} is the *i*th component of the wind tunnel estimated spectral POD mode; χ_l is the corresponding spectral eigenvalue; $\theta_{il}(\omega_k;\alpha) = \tan^{-1}\left(\frac{\text{Im}(\Upsilon_{il})}{\text{Re}(\Upsilon_{il})}\right)$ is the phase angle; N_l is the total number of modes used in the representation; $\hat{\theta}_{lk}$ is the random phase angle that follows a uniform distribution in $[0,2\pi]$ and generates the wind load stochasticity; $\omega_k = k\Delta\omega$ with $\Delta\omega$ the frequency discretization step size; N_k is the total number of frequency steps of the discretization; and w_1 , w_2 , and w_3 are random variables modeling the uncertainty that exist in estimating Υ_{il} and χ_l from wind tunnel data. Lastly, to ensure reasonable initial and final conditions, each realization of $\mathbf{F}(t; v_H, \alpha)$ is generally multiplied by an envelope function that linearly ramps the first and last two minutes of the load history [17, 22, 12].

4.3. Stochastic simulation scheme for reliability estimation

Following the sector-by-sector approach, the problem of estimating the failure probability, P_f , of the system reduces to solving Eq. (29) for each sector and then taking, P_f , as the maximum sectorial failure probability, i.e., as:

$$P_f = \max_{1 \le s \le N_s} [P_{f_s}] \tag{33}$$

where P_{f_s} is the failure probability in sector s and N_s is the total number of wind sectors. As outlined in [12], P_{f_s} can be efficiently solved for small failure probabilities through Monte Carlo methods based on stratifying in terms of the v_H and therefore writing P_{f_s} as:

$$P_{f_s} = \sum_{i=1}^{N_e} P(g(\mathbf{Z} < 0)|s, E_{v_H,i}) P(E_{v_H,i})$$
(34)

where: $E_{v_H,i}$ the *i*th interval of a mutually exclusive and collectively exhaustive partitioning of the wind speed axis; N_e is the total number of intervals in the partition; $P(g(\mathbf{Z} < 0)|s, E_{v_H,i})$ is the probability of limit state violation condition on wind speeds belonging to sector s and wind speed interval $E_{v_H,i}$; while $P(E_{v_H,i})$ is the probability of v_H belonging to $E_{v_H,i}$ that can be directly estimated from CCDF of Eq. (31). It should be observed that the formulation of Eq. (34) is based on the assumption that $P(E_{v_H,i})$ is known with sufficient accuracy. Basically, the stratification of Eq. (34) is advantageous as it reduces the estimation of P_{fs} to the estimation of a series of conditional probabilities, $P(g(\mathbf{Z} < 0)|s, E_{v_H,i})$, that are no longer rare event problems and can therefore be solved using standard Monte Carlo methods. As discussed in [12], the efficiency of the scheme depends on the stratification, and therefore the wind speed intervals $E_{v_H,i}$. An effective approach for their definition is to first observe that the lower bound of the first interval, $v_{H,1}^L$, must be zero while the upper bound of the last interval, v_{H,N_e}^L , must be infinity. The remaining bounds can then be defined by specifying an equal increment of the square of wind speed, $(v_{H,i}^U)^2 - (v_{H,i}^L)^2 = (v_{H,N_e}^L)^2/(N_e - 1)$, and fixing v_{H,N_e}^L based on the expected/target failure probabilities associated with the limit states. In general, experience suggests eight to ten intervals are sufficient [41, 42].

4.4. Integration with AFNA

In integrating the AFNA scheme with the stochastic simulation scheme of Sec. 4.3, elastic solutions for all samples are first obtained through modal analysis (Eq. 8), based on which the multipliers s_e and s_p can be efficiently evaluated as outlined in Sec. 2.2. Subsequently, the AFNA scheme is used to estimate the inelastic response time histories for all samples in which inelasticity occurs (i.e., $s_e < 1$). It is important to note that, unlike the strain-based scheme used in the framework outlined in [12], the AFNA scheme is capable of accurately estimating responses for both shakedown and non-shakedown samples. Therefore, in estimating the probabilities associated with exceeding any displacement-based limit state, these will no longer be conditioned on the system reaching the state of shakedown, i.e., the failure probabilities and associated distribution functions will fully capture behavior subsequent to shakedown. In addition, for each sample of the simulation full responses time histories are generated for the displacements, velocities, and accelerations at all degrees of freedom, as well as hysteretic behaviors including deformations and forces at all integration points of the discretization, therefore providing a far more comprehensive picture of the inelastic response of the structural system at and beyond the state of dynamic shakedown.

5. Case Study

5.1. Description

5.1.1. Building system and numerical modeling

A 3D 45-story reinforcement concrete (RC) core building located in New York City and designed by the ASCE 7-22 committee on performance-based wind engineering is considered for this case study. As shown in Fig. 8, the core is composed of multiple shear walls that are connected through the link (coupling) beams at each floor. The total height of the building is 180.6 m, with a story height of 4 m. The concrete compressive strength, f'_c , reinforcement strength, f_y , modal damping ratios, ξ_l , dead loads, D, and "arbitrary point-in time" live loads, L_{apt} , are all considered as random variables with the characteristics summarized in Table 2. In addition, a nominal perimeter cladding surface load of 1.2 kN/m was considered. The Young's modulus of the concrete, which is considered of normal strength, is assumed to be given by $E_c = 4700\sqrt{f'_c}$ (Mpa) and is therefore a derived random variable.

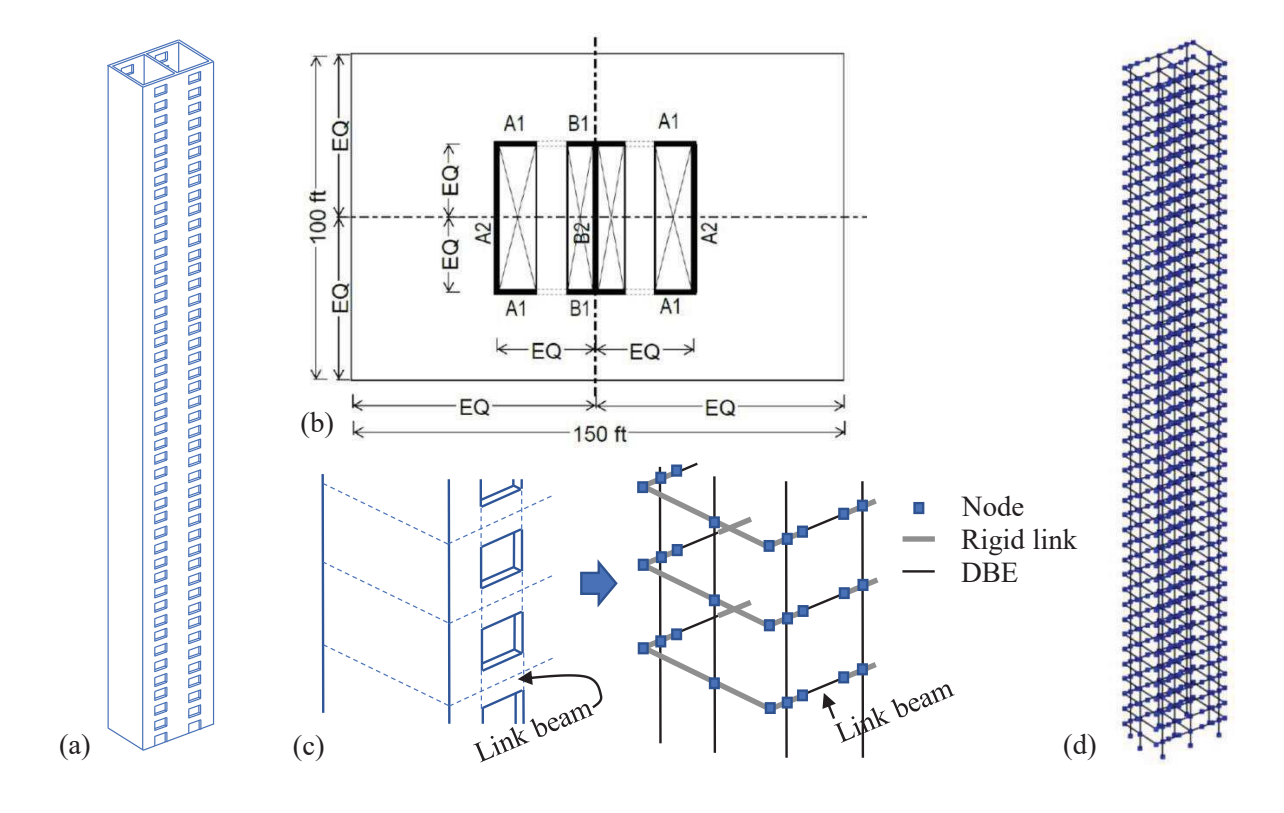


Figure 8: The case study building: (a) Core; (b) Plan view; (c) Modeling strategy; (d) 3D finite element model.

In developing the finite element model of the structure, rigid diaphragm constraints were used to model the in-plane stiffness of each floor. The shear walls were modeled using equivalent columns (modeled with displacement-based beam-column elements) and rigid links, as

Table 2: Description of random variables considered for the 45-story reinforced concrete building.

	Nominal	Mean Nominal	CoV*	Distribution	Reference
r/	69 (MPa)	1.09	0.11	Normal	[43]
f_c'	83 (MPa)	1.08	0.11	Normal	[43]
f_y	414 (MPa)	1.13	0.03	Normal	[43]
ξ_l	2%	1	0.4	Lognormal	[44]
D	-	1.05	0.1	Normal	[39, 40]
L_{apt}	-	0.24	0.6	Gamma	[39, 40]
w_1	1.0	1.0	0.075**	Normal	[45]
w_2	1.0	1.0	0.05	Normal	[46]
w_3	1.0	1.0	0.05	Normal	[46]

^{*} CoV: coefficient of variation.

Table 3: Nominal floor loads of the 45-story reinforced concrete building.

Self Load [kN/m ²]	Superimposed Dead Load $[kN/m^2]$	Live Load [kN/m ²]
2.39	0.72	3.11

illustrated in Fig. 8. To properly model the torsional stiffness of the building, the rotational constraints at the ends of each rigid link are released. The link beams were modeled with displacement-based beam-column elements. All the displacement-based beam-column elements had five integration points. The natural frequencies of the first three modes were $f_1 = 0.246$ Hz, $f_2 = 0.305$ Hz, and $f_3 = 1.01$ Hz when all random variables assumed their nominal values and the structure is modeled as linear elastic. In addition, 3D piecewise linear yield surfaces with 32 surfaces were considered for modeling the yield domains associated with each shear wall and link beam section. Geometric nonlinearity was considered through the linearized P-Delta model outlined in Sec. 3.3. The subsequent modeling and new developments were carried out in WiRA (Wind Reliability Analysis), a standalone freeware application of the Resilient and Efficient Structures Laboratory (RESLab) that is freely downloadable at: https://reslab.engin.umich.edu/wira-software.

^{**} Related to record duration, takes 0.075 since the full-scale loads have a duration of 1 hour.

5.1.2. Wind loads

The stochastic wind loads were generated through the application of the wind tunnel informed spectral POD model outlined in Sec. 4.2.3. Wind tunnel data, provided by Cermak Peterka Petersen (CPP), was collected through the instantaneous measurement of pressures on the surface of a 1:400 scale building model. Data was collected for 131.04 s at a sampling frequency of 250 Hz and 36 wind directions, $\alpha = \{0^{\circ}, 10^{\circ}, ..., 340^{\circ}, 350^{\circ}\}$. Through appropriate scaling based on Strouhal number matching and integration to the floor centers, the data provided an experimental realization of the two translational forces and torsional moment (about a vertical axis) acting at the center of mass of each floor. It should be noted that, although the Strouhal number matching is well-established and widely used, it unavoidably introduces errors owing primarily to the violation of the Reynolds number similarity requirement. However, for bluff bodies, and therefore the majority of buildings, these errors are generally negligible [47]. From the cross-power spectral density of this data, the first five frequency-dependent spectral POD modes and eigenvalues were estimated and used to calibrate the stochastic wind load model of Eq. (32). In particular, given a mean hourly wind speed of interest, v_H , and associated direction, α , the model was calibrated to generate realizations of the vector-valued stochastic wind loads, $\mathbf{F}(t; v_H, \alpha)$, with a total duration of 3840 s with a sampling frequency of 2 Hz. The loads were subsequently modified by first ramping up/down the first/last 2 minutes and then multiplying by w_1 , w_2 , and w_3 to account for the uncertainties in the wind tunnel experiments due, respectively, to the finite length of the wind tunnel data, the use of scale models, and the presence of observational errors. The probabilistic properties of w_1 , w_2 , and w_3 are reported in Table 2.

To characterize the intensity of wind events, the probability distribution of the site-specific annual largest non-directional mean hourly wind speed is required. This was estimated from the point values of the 3 s gust wind speeds, v_{3s} , reported in the wind speed maps of the ASCE 7-22 for the mean recurrence intervals of: 300, 700, 1700, 3000, 10000, 100000, and 1000000 years. These were transformed to site-specific mean hourly wind speeds through the expression:

$$v_H = \bar{b} \left(\frac{H}{10}\right)^{\bar{\alpha}} v_{3s} \tag{35}$$

where \bar{b} and $\bar{\alpha}$ are terrain exposure constants respectively taken as 0.45 and 1/4 which cor-

Table 4: Values of LR for different wind direction sectors.

Sector	N	NE	Е	SE	S	SW	W	NW
LR	0.78	0.78	0.7	0.7	0.7	0.78	1	0.84

respond to Exposure Category B [48], while H is the height of the building. The obtained annual mean hourly wind speeds were subsequently fit to a Weibull distribution. This distribution was subsequently transformed, based on the classic assumption of independent maximum annual wind speeds, to the distribution function of the mean hourly speeds to occur in an observation period of 50 years, lifespan over which the reliability analysis will be carried out. The resulting non-directional hazard curve is shown in Fig. 9.

As outlined in Sec. 4.2.3, the sector-by-sector method is adopted for accounting for wind directionality. In calibrating the approach, eight wind sectors were considered. As illustrated in Fig. 10, the sectors coincided with the compass directions: N, E, S, W, NE, SE, SW, and NW. In particular, the mean hourly wind speed occurring in a given sector, \tilde{v}_H , was linearly related to the non-directional site-specific mean hourly wind speed, v_H , as:

$$\tilde{v}_H = \sqrt{LR}v_H \tag{36}$$

where LR is a location-specific load ratio. Values of the load ratio for New York City were provided by CPP and are reported in Table 4. The uncertainty in the wind direction within a given sector was modeled by considering α as uniformly distributed in each sector.

5.2. Reliability analysis

In calibrating the AFNA-based reliability analysis of Sec. 4, the stratified sampling scheme was based on dividing the hazard curve into $N_E = 8$ wind speed strata, $E_{v_H,i}$, of equal squared wind speed difference, as illustrated in Fig. 9. The lower bound of the 8th and last strata was calibrated by setting the annual failure probability as 3.0×10^{-5} , which corresponds to the annual failure probability of an ASCE 7-22 Risk Category II building [49]. Using this stratification of the non-directional hazard curve together with the relationship of Eq. (36), 400 samples per sector were used to estimate the failure probability in each sector for a total of 3,200 samples.

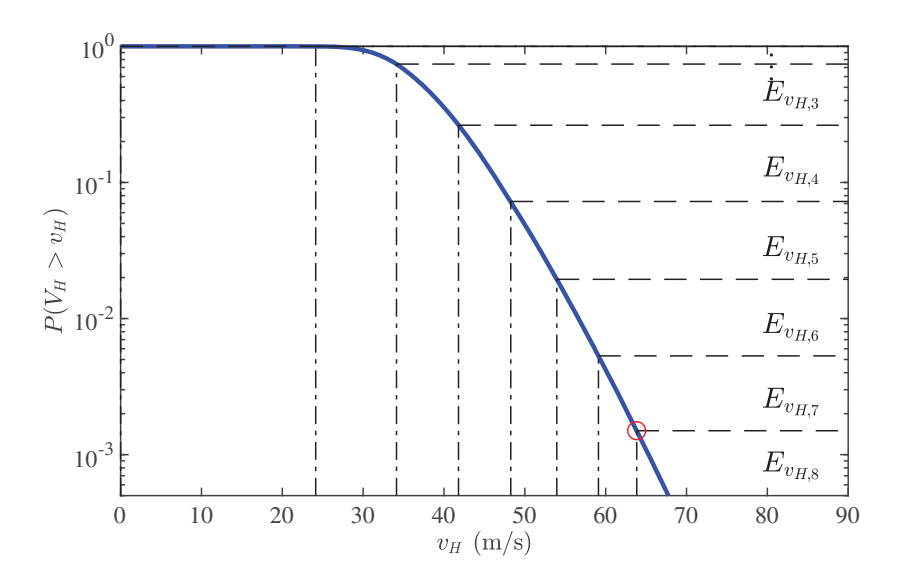


Figure 9: The hazard curve and stratification of the largest 50-year non-directional mean hourly wind speed at the reference height.

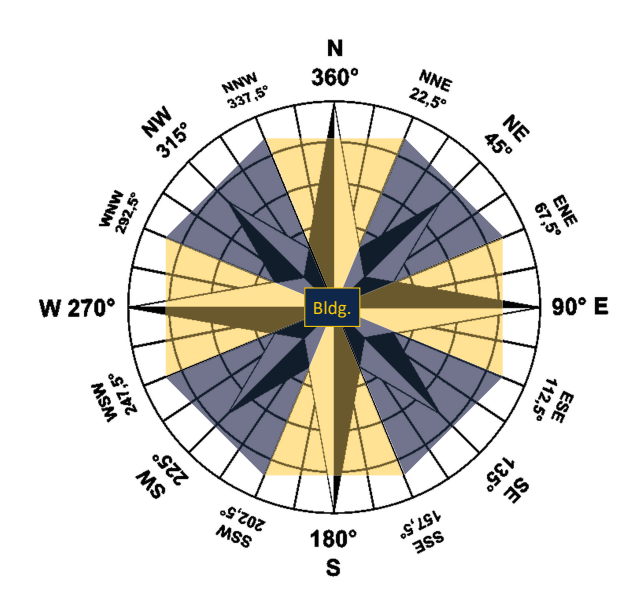


Figure 10: Illustration of wind direction sectors.

Failure probabilities, and associated reliability indices, were estimated for the classes of limit states outlined in Sec. 4.1 and therefore for component yield (LS1), first yield of the structure (LS2); inability to achieve the state of dynamic shakedown (LS3), and exceedance of the following limit states on displacement:

- 1. LS4a: peak interstory drift $\hat{Dr}_{X,i}$ or $\hat{Dr}_{Y,i} \geq h_i/100$;
- 2. LS4b: peak drift at the building top $\hat{X}_{X,45}$ or $\hat{X}_{Y,45} \geq H/200$;
- 3. LS4c: permanent set $\bar{D}r_{X,i}$ or $\bar{D}r_{Y,i} \geq h_i/1000$.

where h_i is the height of the *i*th floor; H is the total height of the structure; while $\hat{Dr}_{X,i}$, $\hat{Dr}_{X,i}$, $\hat{Dr}_{X,i}$, and $\hat{Dr}_{Y,i}$ are respectively the peak interstory drift in the X direction, peak interstory drift in Y direction, residual interstory drift in X direction, and residual interstory drift in Y direction at the *i*th floor. It should be observed that the limit states of LS4b and LS4c are based on those suggested in [1] for the performance objective of Continuous Occupancy. Because no explicit threshold is suggested for peak interstory drift, LS4a was based on discussions with the Authors of [1] and is considered consistent with LS4b.

In estimating the nonlinear responses through the AFNA algorithm, the first three modes were considered as dynamic (i.e., characterized by both a dynamic and background component), with the subsequent three modes considered as background modes, while all remaining modes were considered quasi-static. The initial time step was taken as $\Delta t = 0.5$ s. In the adaptive process, the scaling factor ν for identifying nonlinearity was taken as 0.9. The time step modifier, η , was taken as an integer such that the modified time step, $\Delta t/\eta$, was less than or equal to 1/4 of the third dynamic modal period considered in the analysis. The tolerance for the convergence of the nonlinear correction forces was set to $e_{F_{NLC}} = 1 \times 10^{-6}$.

5.3. Results

5.3.1. Preamble

The results obtained through the reliability analysis are discussed in this section. In particular, the responses of a representative shakedown and non-shakedown sample are first discussed in detail. The responses of the shakedown sample obtained through AFNA are verified by comparing them with those obtained from the strain-driven stress resultant dy-

namic shakedown scheme [21, 22, 12]. Second, the resulting reliability indices and exceedance probabilities are discussed.

5.3.2. Responses of representative samples

To illustrate the capability of the AFNA scheme for efficiently simulating a full range of response time histories for both shakedown and non-shakedown samples, two such samples are discussed here. In particular, the shakedown sample is for a wind direction of $\alpha = 280^{\circ}$ and wind speed $\tilde{v}_H = 65.22$ m/s (mean recurrence interval (MRI) = 10981 years). The multipliers for this sample are $s_e = 0.83$ and $s_p = 1.16$. The peak and residual interstory drifts obtained through the strain-driven stress resultant shakedown scheme outlined in [12] and AFNA are comparatively shown in Fig. 11. It is observed that both the peak and residual interstory drifts by the two schemes are consistent. The residual interstory drifts by AFNA are smaller than those of the strain-driven stress resultant shakedown scheme. This can be traced back to how the strain-driven shakedown schemes estimate the asymptotic response under an infinitely repeated wind load [21, 22, 12], which will in general cause overestimation, while the AFNA scheme provides estimates of the actual response from the excitation. In addition, as a step-by-step solution method, the AFNA scheme is capable of estimating the entire response time history, at any degree of freedom or integration point of the discretized system. As an illustration, the roof displacement in the X and Y directions, as well as rotation about the Z direction, are shown in Fig. 12.

The locations of the 68 elements experiencing inelasticity (out of the 585 total displacement-based beam-column elements of the discretization) are shown in Fig. 13(a). Among the integration points experiencing inelasticity, the 1st integration point of the 4th element is selected as representative. Fig. 13(b) reports the section deformation and forces, including axial deformation ϵ_x and force N_x , curvatures κ_y , κ_z and moments M_y , M_z where the inelastic response is clearly visible. Fig. 13(c) illustrates how the force $N_x - M_y - M_z$ trajectory moves within the 3D yield domain as the proposed AFNA scheme finds the solution considering yielding in the 3D domain with plastic deformations governed by the associated flow rule. Fig. 13(c) also illustrates how yielding occurs with respect to the yield domain of the selected integration point. Similar information is also available for any integration point of

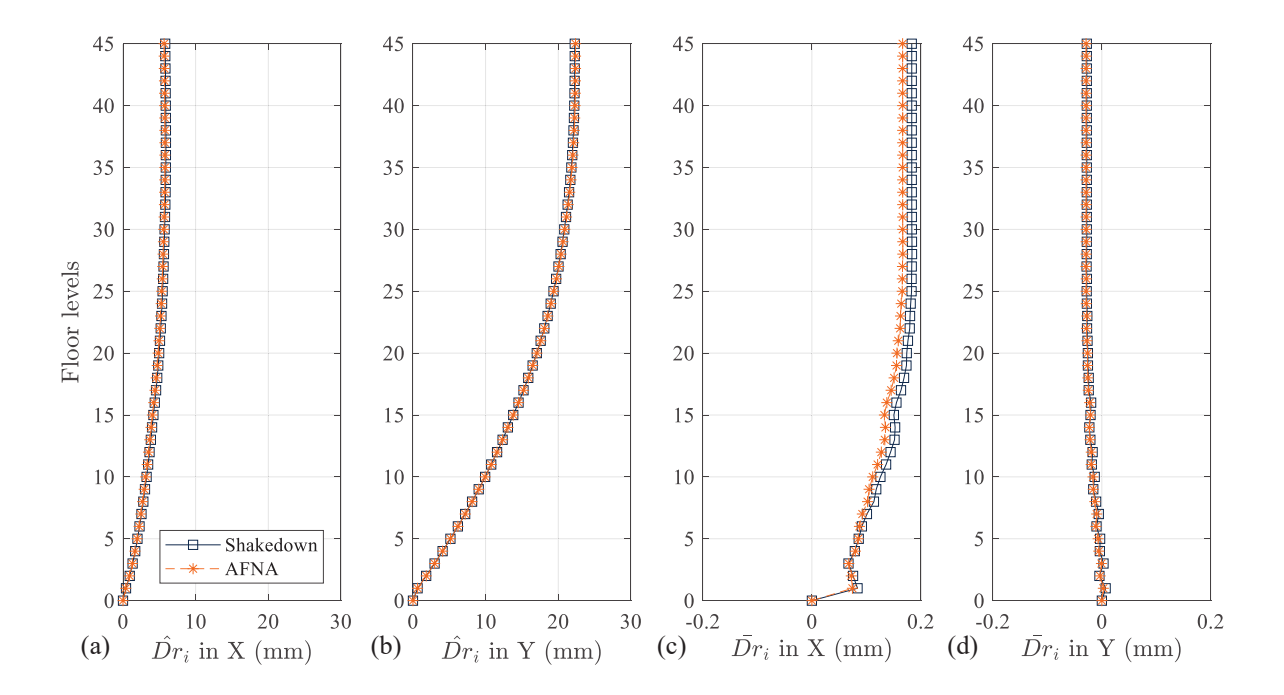


Figure 11: Comparison of the peak (a)-(b) and residual (c)-(d) interstory drifts in the X and Y directions obtained from the stress resultant shakedown and AFNA schemes.

interest. Moreover, in addition to the full range of response time histories and hysteretic curves, the AFNA scheme exhibited high efficiency requiring only 16.16 s to find the solution, which is considerably less than the 124.15 s taken by the strain-driven stress resultant shakedown approach (times estimated using a personal computer with Intel(R) Core(TM) i7-8700 @ 3.20 GHz processor).

The strain-based shakedown scheme is not capable of estimating inelastic responses for non-shakedown samples. The responses of these samples, however, can be solved by the AFNA scheme. This enables the AFNA approach to analyze samples with strong inelasticity and facilitates the estimation of reliabilities associated with limit states that are closer to incipient collapse. To illustrate this, a strongly inelastic non-shakedown sample, caused by wind loading with $\alpha=270^{\circ}$ and $\tilde{v}_H=64.35$ m/s (MRI = 8917 years), is discussed in the following. The multipliers of this sample were $s_e=0.41$ and $s_p=0.60$. Fig. 14 shows the nonlinear modal hysteretic curves, i.e., Y_i vs $\phi_i^{\rm T} F_{\rm NL}$, for the three dynamic modes considered in the analysis. This provides a clear picture of the global inelastic behavior of the system and is an output that is exclusive to the AFNA approach (i.e., traditional step-by-step integration schemes do not provide this information as they are not based on model decomposition). In

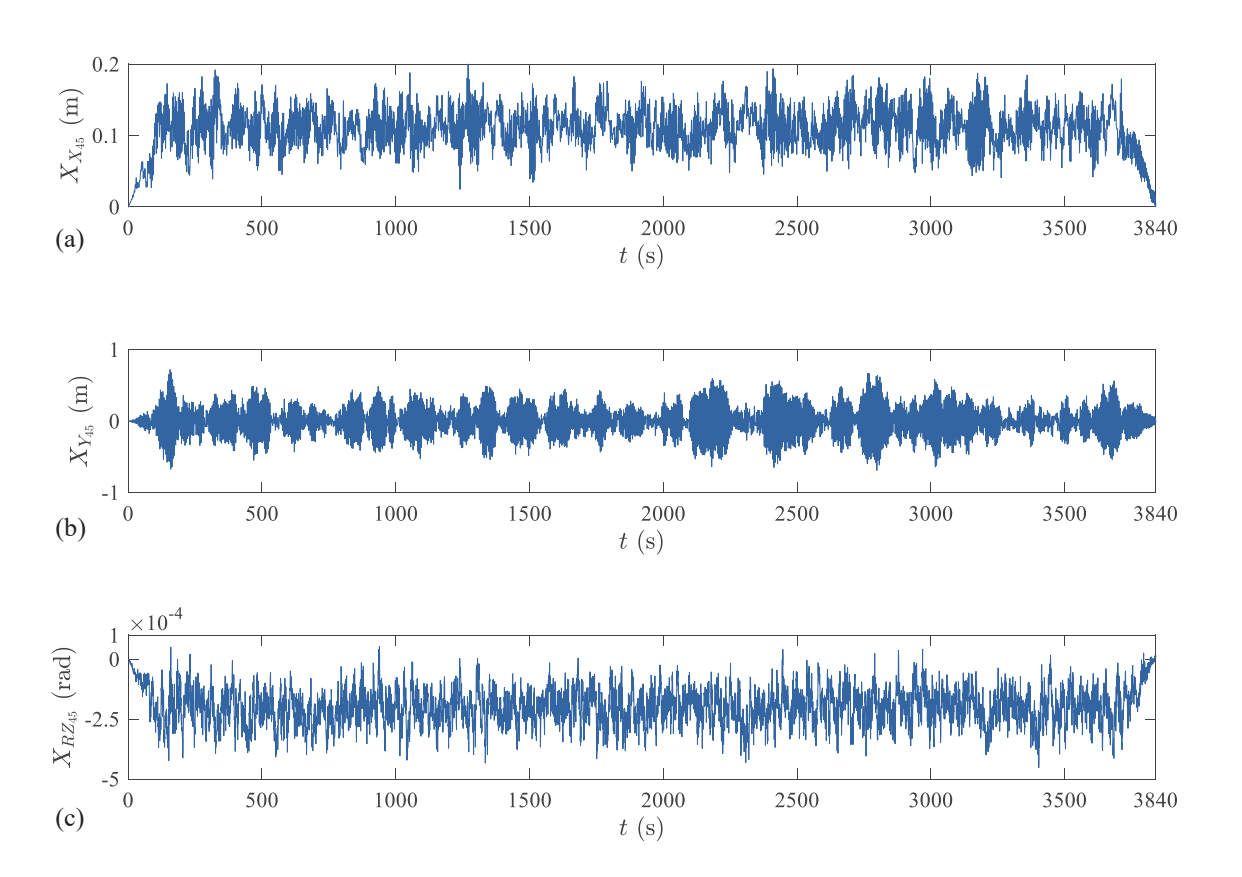


Figure 12: Time history of roof displacement estimated by AFNA in: (a) X direction; (b) Y direction; and (c) rotation about the Z direction.

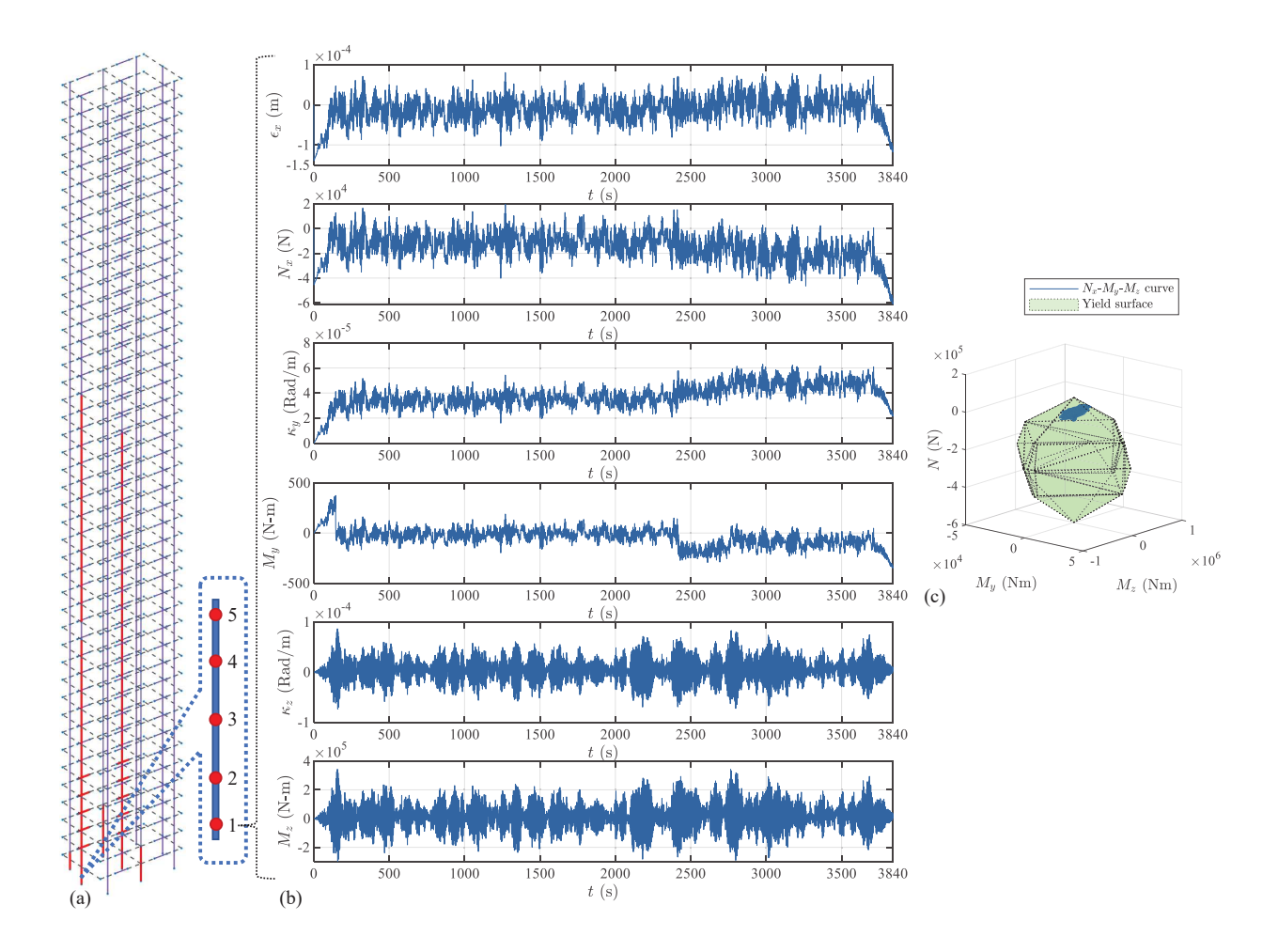


Figure 13: (a) Location of the nonlinear elements (marked in red); (b) time histories of section deformations and forces; and (c) 3D yield domain and trajectory of $N_x - M_y - M_z$, estimated by AFNA at the 1st integration point (red points in (a)) of the 4th element.

particular, it can be seen that all three modes have observable inelasticity, with the second mode exhibiting extremely strong nonlinearity with significant residual deformation. The peak and residual interstory drifts are shown in Fig. 15. It is observed from Fig. 15(c) that the residual interstory drift is large and close to the peak value of Fig. 15(a). This is consistent with Fig. 16, where, compared to the dynamic component of the roof displacement in X direction, the residual component is dominant and accumulates throughout the entire history indicating a ratcheting type failure of the system. In total 411 out of the 585 displacement-based beam-column elements experienced inelasticity, as illustrated in Fig. 17(a). Fig. 17(b) reports the section deformations and forces at the 1st integration point of the 4th element. These include the axial deformation ϵ_x and force N_x , curvatures κ_y and κ_z , and moments

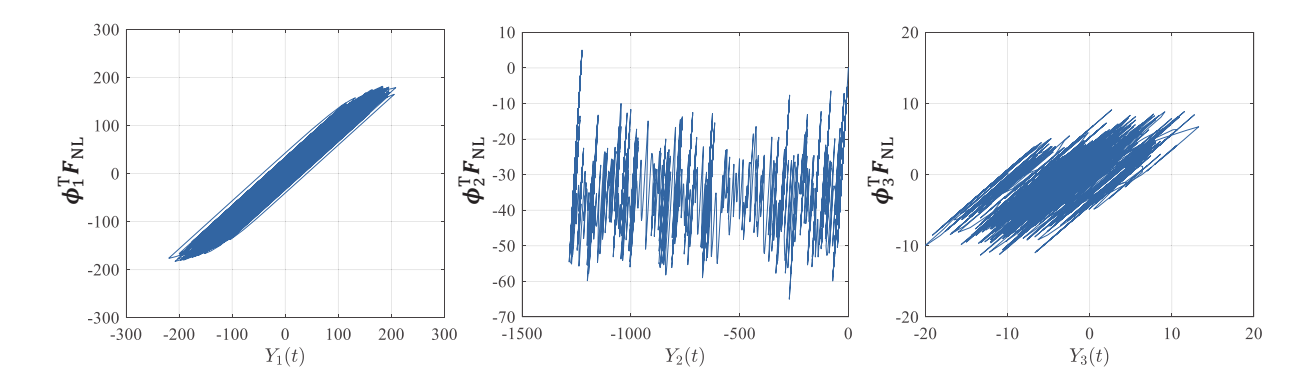


Figure 14: The nonlinear modal hysteretic curves, Y_i vs $\phi_i^{\mathrm{T}} \mathbf{F}_{\mathrm{NL}}$, of the three nonlinear dynamic modes.

 M_y , M_z . Consistent with the observation concerning the roof displacement response in the X direction, this element has experienced extreme axial deformation and bending about the local y axis that is accumulating with time. In addition, Fig. 13(c) shows how the force $N_x - M_y - M_z$ trajectory moves on the yield surface and how yielding occurs with respect to the yield domain of the selected integration point. It is worth noting that even for this strongly nonlinear non-shakedown sample, the AFNA algorithm is still capable of simulating a full range of response time histories, including global displacements as well as local hysteretic curves. This not only extends the range of responses that can be used in reliability analysis, as compared to the strain-driven stress resultant shakedown scheme, but also provides vital insights into the response of individual samples.

5.3.3. Reliability results

With response samples estimated through the AFNA algorithm, reliability indices for component-level yield (LS1), system-level first yield (LS2), inability to reach the state of dynamic shakedown (LS3), as well as the displacement-based limit states (LS4) of Sec. 5.2 were estimated and are summarized in Table 5. It is seen that some reliability indices, e.g., for LS1 and LS2, are smaller than 3.0, the target reliability for the archetype building of this case study. Notwithstanding how the system does not meet the target component reliability, it is interesting to observe how the building has a reliability index of nearly 3.3 at dynamic shakedown. This illustrates how the system has an important plastic reserve in which controlled inelasticity can occur without risk of potential failure due to low cycle fatigue and ratcheting as the state of dynamic shakedown occurs which, by definition, excludes the

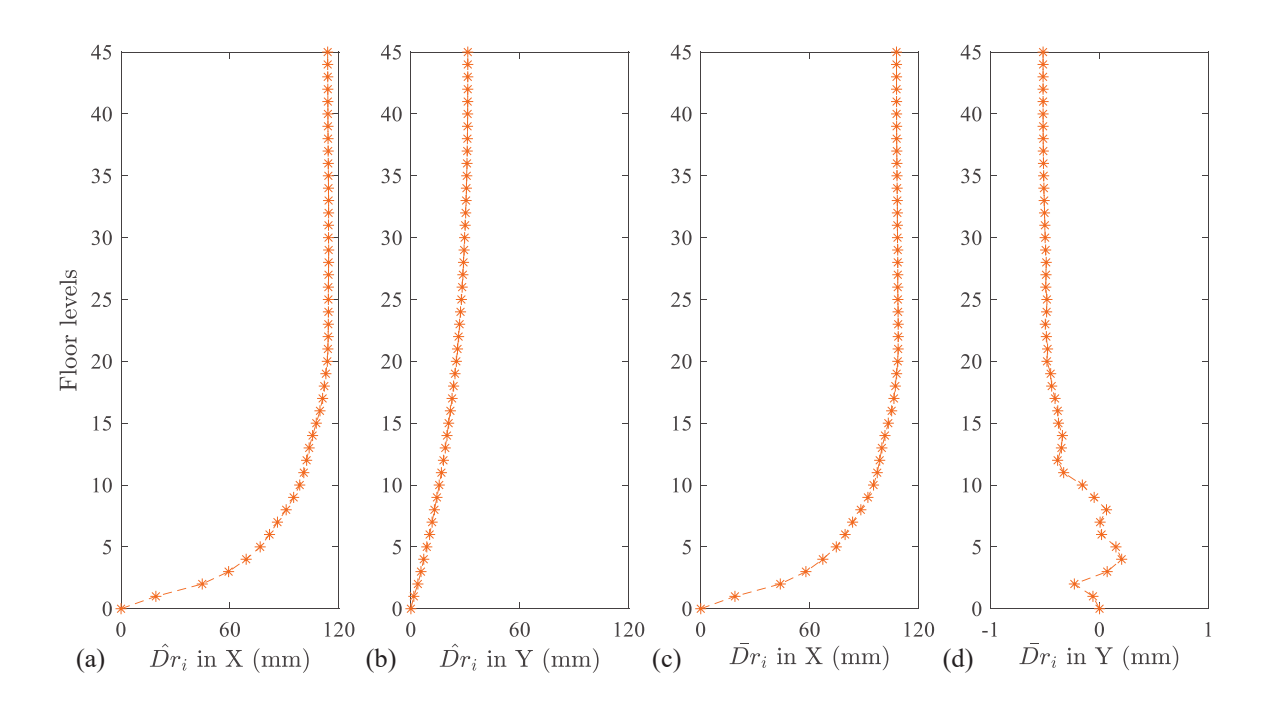


Figure 15: Peak (a)-(b) and residual (c)-(d) interstory drifts in the X and Y directions by AFNA.

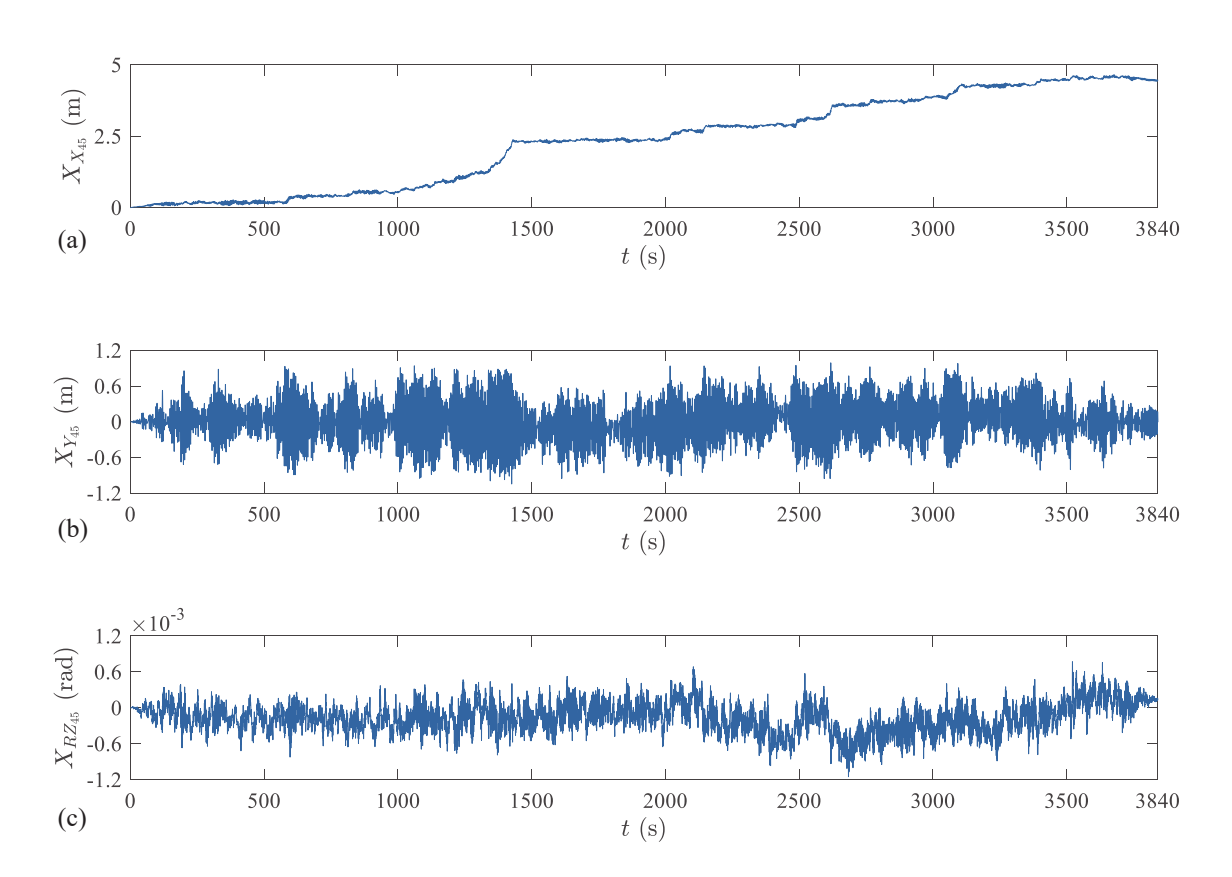


Figure 16: Time history of roof displacement in: (a) X direction; (b) Y direction; and (c) rotation about Z direction by AFNA.

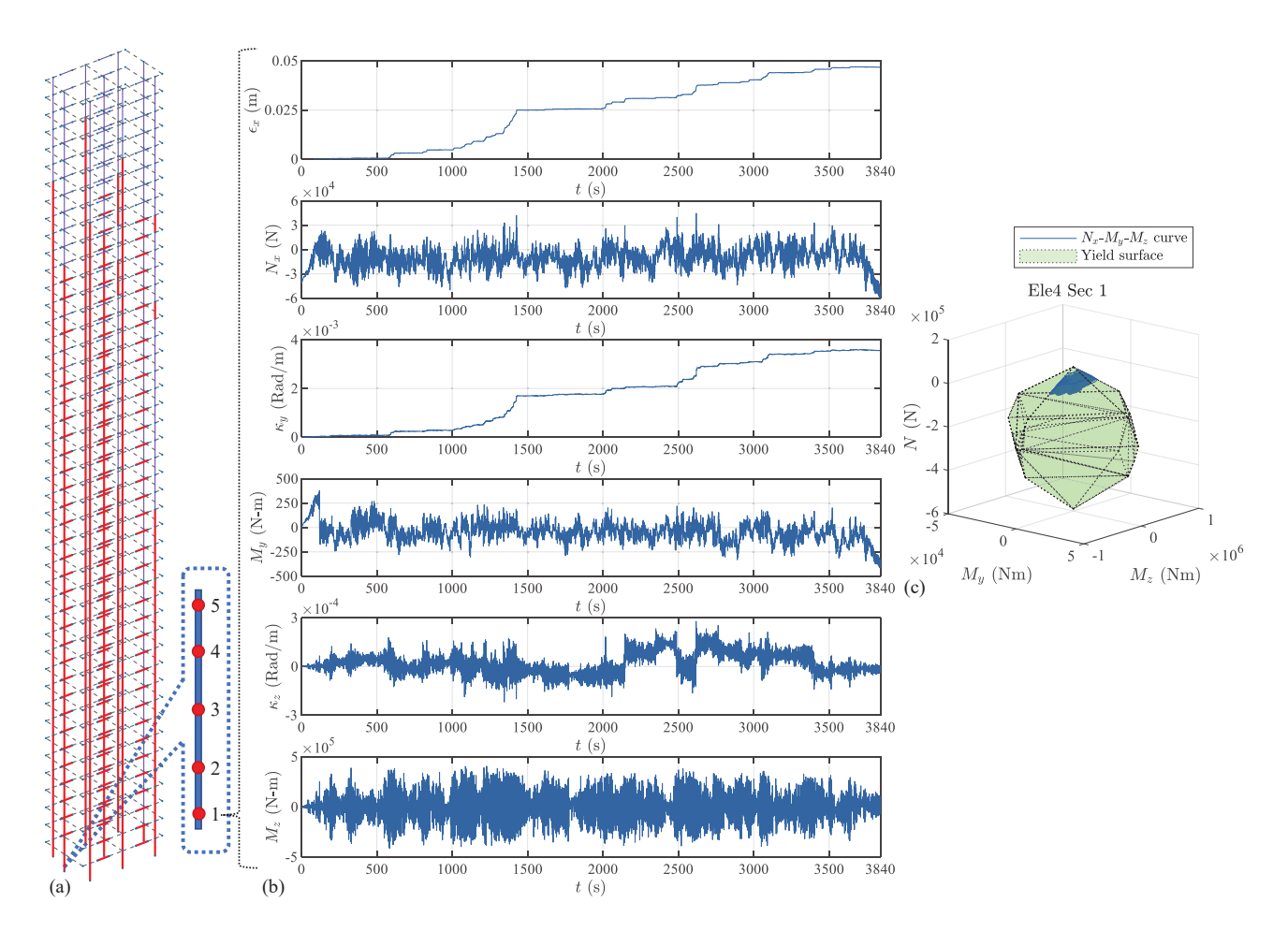


Figure 17: (a) Location of nonlinear elements (marked as red); (b) time histories of section deformations and forces; and (c) 3D yield domain and trajectory of $N_x - M_y - M_z$, estimated by AFNA at the 1st integration point (red points in (a)) of the 4th element.

possibility of such failure [7, 21].

Fig. 18 reports the conditional (on shakedown occurring) and non-conditional exceedance probability curves (EPCs) for the residual interstory drifts at the critical floors as well as the peak roof drift in the X and Y directions estimated from the AFNA scheme and, when possible, the strain-driven stress resultant dynamic shakedown scheme outlined in [12]. By comparing the conditional EPCs of the critical peak and residual interstory drifts of Figs. 18(a)-(d), the validity of the AFNA scheme can be clearly seen. Indeed, as would be expected, both approaches give near identical peak interstory drift conditional EPCs, which is dominated by the elastic part of the response, with, however, the residual drift conditional EPCs estimated from AFNA providing smaller exceedance probabilities due to the asymp-

totic nature of the strain-driven scheme. The sudden change in the conditional EPCs seen in Fig. 18(d) is a direct consequence of the implementation of the sector-by-sector approach where a change in the critical sector occurs. Similar results for the conditional EPCs of the peak roof drift can be seen in Figs. 18(e)-(f).

Concerning the non-conditional EPCs, which are not available for the strain-driven scheme, the effect of including the non-shakedown samples is clearly evident. Indeed, from Figs. 18(c)-(d), significantly higher exceedance probabilities are seen for the critical residual interstory drifts. In addition, from Fig. 18(a) and Fig. 18(e), the residual deformation occurring in events in which dynamic shakedown does not occur can clearly lead to large increases in inelastic deformation as the system nears collapse. The estimation of these inelastic deformations allows for the direct evaluation of performance beyond the state of dynamic shakedown, an aspect not contemplated by the strain-driven shakedown schemes which, therefore, lack insight into the sensitivity of the inelastic response of the system to load increments beyond the state of dynamic shakedown. Nevertheless, these results do confirm how the state of dynamic shakedown ensures the controlled nature of the inelastic deformation occurring in the system and therefore its use as a system-level performance objective for practical implementation of performance-based wind design. The possibility to directly estimate this information, while also estimating the reliability associated with the state of dynamic shakedown without loss of efficiency as compared to the strain-driven scheme outlined in [12]), highlights the potential of the proposed AFNA scheme of this work.

6. Summary and conclusions

In this paper, an efficient adaptive fast nonlinear analysis (AFNA) integration scheme was proposed as a powerful alternative to the recently introduced strain-driven dynamic shakedown method. The scheme was derived within the setting of stress resultant distributed plasticity. The method is based on a step-by-step iterative solution process over the entire duration of the dynamic load history, therefore providing a full range of global and local response time histories for scenarios both below and above the state of dynamic shakedown. By developing the scheme within the context of shakedown analysis, the evaluation of the state of dynamic shakedown is naturally encompassed. The scheme is integrated within a

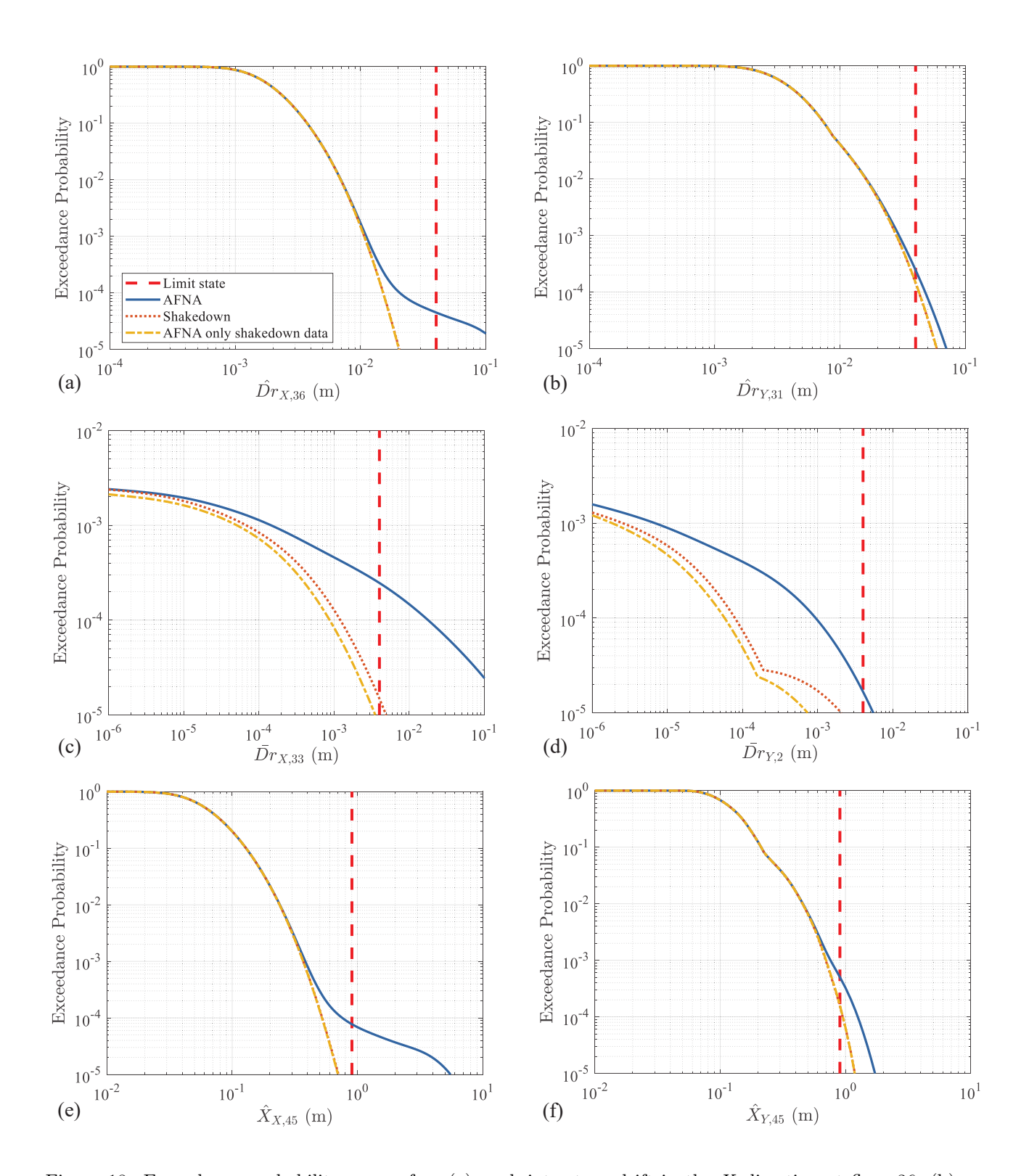


Figure 18: Exceedance probability curves for: (a) peak interstory drift in the X direction at floor 36; (b) peak interstory drift in the Y direction at floor 31; (c) residual interstory drift in the X direction at floor 33; (d) residual interstory drift in the Y direction at floor 1; (e) peak roof drift in the X direction; and (f) peak roof drift in the Y direction.

Table 5: Failure probabilities and reliability indices for the archetype building.

Limit state	Description	Failure probability	Reliability index	
LS1	First component yield	0.0026	2.80	
LS2	First system yield	0.0029	2.76	
LS3	Non-shakedown	$5.12{ imes}10^{-4}$	3.28	
LS4a	$\hat{Dr}_i \ge h_i/100$ in X	4.49×10^{-5}	3.92	
	$\hat{Dr}_i \ge h_i/100$ in Y	4.05×10^{-4}	3.35	
LS4b	$\hat{X}_{X,45} \ge H/200$	7.73×10^{-5}	3.78	
	$\hat{X}_{Y,45} \ge H/200$	5.05×10^{-4}	3.29	
LS4c	$\bar{Dr}_i \ge h_i/1000$ in X	$2.46{ imes}10^{-4}$	3.48	
	$\bar{Dr}_i \ge h_i/1000$ in Y	7.56×10^{-5}	3.79	

recently developed stochastic simulation framework therefore allowing direct propagation of uncertainty. This enables the assessment of the reliability against limit states ranging from component first yield, through dynamic shakedown, to incipient collapse. A full-scale 3D archetype reinforced concrete tower subject to extreme winds was considered as a case study for illustration. The AFNA scheme was seen to estimate, without loss of efficiency, inelastic responses that are consistent in terms of accuracy with the recently proposed strain-driven dynamic shakedown method. The capability of the scheme to estimate the probabilistic distributions associated with a full range of inelastic responses beyond shakedown was illustrated.

Acknowledgements

This research effort was supported in part by the National Science Foundation (NSF) under Grant No. CMMI-1750339 and the Magnusson Klemencic Associates (MKA) Foundation under RGA #A101.1. This support is gratefully acknowledged.

References

[1] ASCE, . Prestandard for Performance-Based Wind Design. American Society of Civil Engineers (ASCE), Reston, VA; 2019.

- [2] Ciampoli, M., Petrini, F., Augusti, G.. Performance-Based Wind Engineering: Towards a general procedure. Struct Saf 2011;33(6):367–378.
- [3] Petrini, F., Ciampoli, M.. Performance-based wind design of tall buildings. Struct Infrastruct E 2012;8(10):954–966.
- [4] Barbato, M., Petrini, F., Unnikrishnan, V.U., Ciampoli, M.. Performance-Based Hurricane Engineering (PBHE) framework. Structural Safety 2013;45:24–35.
- [5] Caracoglia, L.. A stochastic model for examining along-wind loading uncertainty and intervention costs due to wind-induced damage on tall buildings. Engineering Structures 2014;78:121–132.
- [6] Beck, A.T., Kougioumtzoglou, I.A., dos Santos, K.R.M.. Optimal performance-based design of non-linear stochastic dynamical RC structures subject to stationary wind excitation. Engineering Structures 2014;78:145–153.
- [7] Chuang, W.C., Spence, S.M.J.. A performance-based design framework for the integrated collapse and non-collapse assessment of wind excited buildings. Engineering Structures 2017;150:746–758.
- [8] Cui, W., Caracoglia, L.. A unified framework for performance-based wind engineering of tall buildings in hurricane-prone regions based on lifetime intervention-cost estimation. Struct Saf 2018;73:75–86.
- [9] Ouyang, Z., Spence, S.M.J.. A performance-based wind engineering framework for envelope systems of engineered buildings subject to directional wind and rain hazards. Journal of Structural Engineering 2020;146(5):04020049.
- [10] Cui, W., Caracoglia, L.. Performance-based wind engineering of tall buildings examining life-cycle downtime and multisource wind damage. J Struct Eng 2020;146(1).
- [11] Ouyang, Z., Spence, S.M.J.. Performance-based wind-induced structural and envelope damage assessment of engineered buildings through nonlinear dynamic analysis. Journal of Wind Engineering and Industrial Aerodynamics 2021;208(1):104452.

- [12] Chuang, W.C., Spence, S.M.J.. A framework for the efficient reliability assessment of inelastic wind excited structures at dynamic shakedown. Journal of Wind Engineering and Industrial Aerodynamics 2022;220:104834.
- [13] Petrini, F., Francioli, M.. Next generation powe: Extension of the sac-fema method to high-rise buildings under wind hazards. Struct Saf 2022;99:102255.
- [14] Arunachalam, S., Spence, S.M.J.. A stochastic simulation scheme for the estimation of small failure probabilities in wind engineering applications. In: Proc. of European Safety and Reliability Conference (ESREL 2021). 2021,.
- [15] Vickery, B.J.. Wind action on simple yielding structures. Journal of Engineering Mechanics Division 1970;96:107–120.
- [16] Tamura, Y., Yasui, H., Marukawa, H.. Non-elastic responses of tall steel buildings subjected to across-wind forces. Wind and Structures 2001;4(2):147–162.
- [17] Judd, J., Charney, F.. Inelastic behavior and collapse risk for buildings subjected to wind loads. In: Ingraffea, N., Libby, M., editors. Structures Congress 2015. April 23-25, Portland, Oregon, USA; 2015, p. 2483–2496.
- [18] Tabbuso, P., Spence, S.M.J., Palizzolo, L., Pirrotta, A., Kareem, A.. An efficient framework for the elasto-plastic reliability assessment of uncertain wind excited systems. Structural Safety 2016;58:69–78.
- [19] Feng, C., Chen, X.. Crosswind response of tall buildings with nonlinear aerodynamic damping and hysteretic restoring force character. Journal of Wind Engineering and Industrial Aerodynamics 2017;167:62–74.
- [20] Feng, C., Chen, X.. Inelastic responses of wind-excited tall buildings: Improved estimation and understanding by statistical linearization approaches. Engineering Structures 2018;159:141–154.
- [21] Chuang, W.C., Spence, S.M.J.. An efficient framework for the inelastic performance assessment of structural systems subject to stochastic wind loads. Engineering Structures 2019;179:92–105.

- [22] Chuang, W.C., Spence, S.M.J.. Probabilistic performance assessment of inelastic wind-excited structures within the setting of distributed plasticity. Structural Safety 2020;84.
- [23] Ghaffary, A., Moustafa, M.M.. Performance-based assessment and structural response of 20-story SAC building under wind hazards through collapse. Journal of Structural Engineering 2021;147(3):04020346.
- [24] Huang, J., Chen, X.. Inelastic performance of high-rise buildings to simultaneous actions of alongwind and crosswind loads. Journal of Structural Engineering 2022;148(2):04021258.
- [25] Arunachalam, S., Spence, S.M.J.. Reliability-based collapse assessment of wind-excited steel structures within performance-based wind engineering. Journal of Structural Engineering 2022;148(9):04022132.
- [26] Vamvatsikos, D., Cornell, C.A.. Incremental dynamic analysis. Earthquake Engineering and Structural Dynamics 2002;31(3):491–514.
- [27] Huang, M.F., Li, Q., Chan, C.M., Lou, W.J., Kwok, K.C.S.. Performance based design optimization of tall concrete framed structures subject to wind excitations. Journal of Wind Engineering and Industrial Aerodynamics 2015;139:70–81.
- [28] Wilson, E.L.. Three-dimensional static and dynamic analysis of structures. Computers and Structures, Inc, Berkeley, CA 1996;.
- [29] Polizzotto, C.. Dynamic shakedown by modal analysis. Meccanica 1984;19:133–144.
- [30] Borino, G., Polizzotto, C.. Dynamic shakedown of structures under repeated seismic loads. Journal of engineering mechanics 1995;121(12):1306–1314.
- [31] Spence, S.M.J., Kareem, A.. Data-enabled design and optimization (DEDOpt): Tall steel buildings frameworks. Computers and Structures 2013;134(12):134–147.
- [32] Hlaváček, I.. A finite element analysis for elastoplastic bodies obeying hencky's law. Aplikace matematiky 1981;26(6):449–461.

- [33] Wilson, E., Habibullah, A.. Static and dynamic analysis of multi-story buildings, including p-delta effects. Earthquake spectra 1987;3(2):289–298.
- [34] McKenna, F., Fenves, G., Scott, M., omputer program OpenSees: Open system for earthquake engineering simulation. Tech. Rep.; Pacific Earthquake Engineering Center, University of California Berkeley; 2013. URL: http://opensees.berkeley.edu.
- [35] Chen, X., Kareem, A.. Proper orthogonal decomposition-based modeling, analysis, and simulation of dynamic wind load effects on structures. Journal of Engineering Mechanics 2005;131(4):325–339.
- [36] Peng, L., Huang, G., Chen, X., Kareem, A.. Simulation of multivariate nonstationary random processes: Hybrid stochastic wave and proper orthogonal decomposition approach. Journal of Engineering Mechanics 2017;143(9).
- [37] Suksuwan, A., Spence, S.M.J.. Optimization of uncertain structures subject to stochastic wind loads under system-level first excursion constraints: A data-driven approach. Computers & Structures 2018;210:58–68.
- [38] Tokyo polytechnic university (TPU) wind pressure database. http://wind.arch.t-kougei.ac.jp/system/eng/contents/code/tpu; 2008.
- [39] Ellingwood, B., MacGregor, J.G., Galambos, T.V., Cornell, C.A.. Probability based load criteria: Load factors and load combinations. Journal of the Structural Division 1982;108:978–997.
- [40] Zhang, H., R.Ellingwood, B., Rasmussen, K.J.. System reliabilities in steel structural frame design by inelastic analysis. Engineering Structures 2014;81:341–348.
- [41] Irwin, P.A., Garber, J., Ho, E.. Integration of wind tunnel data with full scale wind climate. In: 10th Americas Conference on Wind Engineering, American Association of Wind Engineering. 2005, p. 132–135.
- [42] Isyumov, N., Ho, E., Case, P.. Influence of wind directionality on wind loads and responses. Journal of Wind Engineering and Industrial Aerodynamics 2014;133(1):169– 180.

- [43] Nowak, A.S., Collins, K.R.. Reliability of Structures. CRC Press; 2013.
- [44] Healey, J., Wu, S., Murga, M., Structural building response review. NUREG/CR1423, vol. I. US Nuclear Regulatory Commission, Washington, DC; 1980.
- [45] Sadek, F., Diniz, S., Kasperski, M., Gioffrè, M., Simiu, E.. Sampling errors in the estimation of peak wind-induced internal forces in low-rise structures. Journal of Engineering Mechanics 2004;130(2):235–239.
- [46] Bashor, R., Kijewski-Correa, T., Kareem, A.. On the wind-induced response of tall buildings: the effect of uncertainties in dynamic properties and human comfort thresholds. In: 10th Americas Conference on Wind Engineering. 2005, CD-ROM.
- [47] Simiu, E., Yeo, D.. Wind effects on structures: Modern structural design for wind. John Wiley & Sons; 2019.
- [48] ASCE 7-16, . Minimum design loads and associated criteria for buildings and other structures. American Society of Civil Engineers (ASCE), Reston, VA; 2016.
- [49] ASCE 7-22, . Minimum design loads and associated criteria for buildings and other structures. American Society of Civil Engineers (ASCE), Reston, VA; 2022.